Combined thermodynamic - geochemical modeling in metamorphic geology: Boron as tracer of fluid-rock interaction

Matthias Konrad-Schmolke* **and Ralf Halama**

Institute of Earth and Environmental Science, University of Potsdam, Karl-Liebknecht-Str. 24-25, 14476 Potsdam, Germany

* Corresponding author contact information:

Matthias Konrad-Schmolke

University of Potsdam

Institute of Earth and Environmental Science

Karl-Liebknecht-Str. 24-25

14476 Potsdam

E-mail: mkonrad@geo.uni-potsdam.de

Tel: +49-331-977-5854

Fax: +49-331-977-5700

ABSTRACT

Quantitative geochemical modeling is today applied in a variety of geological environments from the petrogenesis of igneous rocks to radioactive waste disposal. In addition, the development of thermodynamic databases and computer programs to calculate equilibrium phase diagrams have greatly advanced our ability to model geodynamic processes. Combined with experimental data on elemental partitioning and isotopic fractionation, thermodynamic forward modeling unfolds enormous capacities that are far from exhausted.

In metamorphic petrology the combination of thermodynamic and trace element forward modeling can be used to study and to quantify processes at spatial scales from µm to km. The thermodynamic forward models utilize Gibbs energy minimization to quantify mineralogical changes along a reaction path of a chemically open fluid/rock system. These results are combined with mass balanced trace element calculations to determine the trace element distribution between rock and melt/fluid during the metamorphic evolution. Thus, effects of mineral reactions, fluid-rock interaction and element transport in metamorphic rocks on the trace element and isotopic composition of minerals, rocks and percolating fluids or melts can be predicted.

Here we illustrate the capacities of combined thermodynamic-geochemical modeling based on two examples relevant to mass transfer during metamorphism. The first example focuses on fluid-rock interaction in and around a blueschist-facies shear zone in felsic gneisses, where fluid-induced mineral reactions and their effects on boron (B) concentrations and isotopic compositions in white mica are modeled. In the second example, fluid release from a subducted slab, the associated transport of B as well as variations in B concentrations and isotopic compositions in liberated fluids and residual rocks are modeled. We compare the modeled results of both examples to geochemical data of natural minerals and rocks and demonstrate that the combination of thermodynamic and geochemical models enables quantification of metamorphic processes and insights into element cycling that would have been unattainable if only one model approach was chosen.

1. Introduction

In geosciences, field-based observations are fundamental for our interpretations of geological processes. Quantitative models, which should be based on these observations, are essential to predict the evolution of geological systems and the outcome of geological processes (Albarède, 1995). As many disciplines in geosciences are faced with the fact that their study target, such as processes in the deep Earth, is either completely inaccessible, or that spatial or temporal scales at which the processes of interest operate do not allow direct observation, numerical and analogue models have become an indispensable tool to study, quantify and predict processes in Earth and environmental sciences. The development of high resolution - high precision analytical techniques to determine chemical and isotopic compositions of rocks and minerals, an increasing number of experimental data and advances in computational resources enhances our ability to simulate Earth processes and to test the results of these models against field-based observations. As demonstrated by Goldschmidt (1954), physicochemical principles determine systematic compositional changes in rocks and minerals and are hence the key to understand geological processes. The combination of thermodynamic and geochemical forward modeling (e.g., Hebert et al., 2009; Kimura et al., 2009, 2010; Konrad-Schmolke et al., 2008b; Nagel et al., 2012) allows a more precise quantification of key geochemical parameters leading to an improved understanding of geodynamic mechanisms and enables to study and predict rates and kinematics of solid/fluid reactions.

1.1. Thermodynamic equilibrium forward modeling in geosciences

Predicting phase and chemical equilibria is extremely important in many industrial applications, such as gas distillation, cement production and the development of functional materials. Therefore, methods of calculation of phase diagrams (CALPHAD) have been successfully developed and constantly improved. Thermodynamic modeling is nowadays more frequently applied to geoscientific problems, although its application is far more complex than most approaches in material sciences. Challenges in geosciences arise from the fact that most geoscientific questions involve thermodynamic treatment of complex solid solution phases in multiphase systems, interaction of liquid and solid phases and consideration of open system behavior. The application of thermodynamic calculations to geoscientific problems became viable with the compilation of extensive datasets for thermodynamic standard state properties (e.g. Helgeson, 1978; Robie and Hemingway, 1995; Holland and Powell, 1998; Berman, 1988; Gottschalk, 1997), reliable equations of state for

geologically relevant phases and conditions (e.g., Kerrick and Jacobs, 1981; Berman, 1988, Stixrude and Lithgow-Bertelloni, 2005; Holland and Powell, 2011) and solid solution formulations for phases of geoscientific interest (e.g., Margules, 1895; van Laar, 1910; Holland and Blundy, 1984; Berman, 1990; Holland and Powell, 2003). Regarding the interpretation of thermodynamic calculations it is noteworthy that although many of the data incorporated in the available databases are based on experiments or have been numerically determined and are internally consistent, raw experimental data on standard state thermodynamic phase properties are still sparse and incomplete. The limited amount of experimental data together with an inappropriate use of thermodynamic variables (e.g., μ_{H2O} (chemical potential of water) vs. n_{H2O} (amount of water)) can result in significant misinterpretations of modeled thermodynamic equilibria in geosciences (Essene 1989, Powell et al., 2005). Therefore, it is of utmost importance that the formulation of the problem to be solved using thermodynamic modeling complies with limitations induced by the uncertainties implicit in the thermodynamic data and that the thermodynamic variables used to extract information from such models are carefully chosen.

In general, two different thermodynamic calculation approaches can be used to determine thermodynamic equilibria ($\Delta G_R = 0$) among fluid and solid phase assemblages:

1) Solving the equilibrium constant (K)

$$0 = \Delta\mu_0 + RT\ln K$$

where R = gas constant (in J K^{-1} mol^{-1}), T = temperature (in K) and $\Delta\mu_0 = \sum_{i=1}^{m} \upsilon_i \mu_i^0$ = free energy change for the reaction for the species in the standard state with μ_i^0 = standard state molar chemical potential of species i and υ_i = stoichiometric coefficient of species i in the reaction. The equilibrium constant is defined as

$$K = \prod_{i=1}^{m} \left(a_i^{\upsilon_i}\right)$$

where a_i = activity of species i.

2) Global Gibbs energy minimization

$$\text{minimize } G = \sum_{i=1}^{m} n_i \mu_i$$

where n_i = molar amount of component i and μ_i = molar chemical potential of the i^{th} component.

Both approaches require knowledge about the Gibbs free energy of pure phases and a mathematical formulation of the relation between composition and activity/chemical potential in solution phases. Consequently, they both rely on thermodynamic data sets, which contain the standard state thermodynamic parameters and equations of state (EOS) for minerals, fluids and gases together with solution model formulations. The approach of solving the equilibrium constant furthermore requires that the phases among which the thermodynamic equilibria are calculated are pre-defined. This approach is widely utilized in aquatic geochemistry because the equilibrium constants of many aqueous reactions can be readily obtained from experiments (see Oelkers et al., 2009, and references therein). Several commercial and open source computer programs, such as PHREEQC (Parkhurst and Appelo, 1999), SUPCRT92 (Johnson et al., 1992) and THERMOCALC (Powell and Holland, 1988), are available for this purpose.

In metamorphic petrology, element fractionation processes, e.g. fractional crystallization (e.g., Spear 1988; Marmo et al., 2002; Konrad-Schmolke et al., 2006; 2008a), water liberation (e.g., Hacker, 2008; Dragovic et al., 2012) and reactive fluid flow (e.g., Ferry and Gerdes 1998; Beinlich et al., 2010) require thermodynamic modeling of chemically open systems (e.g., Korzhinskii, 1965). In such open systems, coexisting phases cannot be predicted a priori – a prerequisite of the equilibrium constant approach – because they are a function of the pressure (P), temperature (T) and chemical (X) evolution of the rock. Therefore, the approach of global Gibbs energy minimization is preferable as it allows the calculation of thermodynamically stable phase assemblages among all phases available in the database. The mathematical treatment of this approach involves (1) finding the phase assemblage with the lowest Gibbs energy among a large number of solid solution phases (so called global Gibbs energy minimum) and (2) finding the tangent plane that touches the G-X curves of all stable solid solution phases, which is prerequisite for finding the thermodynamically stable compositions of solution phases. For both aspects, different mathematical approaches are published (see Koukarri and Pajarre (2011) for a detailed review) and are implemented into a number of commercial and open source software packages, including MELTS (Ghiorso and Sack, 1995; Asimow and Ghiorso, 1998), pMELTS (Ghiorso et al., 2002) PERPLE_X (Connolly, 2005), THERIAK/DOMINO (de Capitani and Brown, 1987) and GEM-Selektor (Kulik et al., 2004; 2013).

Several pioneering works in the 1980s (Spear, 1988; Spear and Menard, 1989; Spear and Selverstone, 1983; Connolly and Kerrick, 1987; de Capitani and Brown, 1987) established the use of Gibbs energy minimization in petrologic modeling. These studies successfully demonstrated modeling of different rock-forming processes utilizing Gibbs energy minimization and yielded new insight into metamorphism. In more recent publications, Gibbs energy minimization was used in a number of different contexts including precise correlations of the pressure-temperature evolution of metamorphic rocks with age determinations (e.g., Pollington and Baxter 2010), fluid-rock and melt-rock interaction (Nagel et al., 2012; Konrad-Schmolke et al., 2011a), deformation (Pearce and Wheeler 2010), fluid expulsion during metamorphic reactions in subduction zones (Dragovic et al., 2012; Connolly, 2005; Kerrick and Connolly, 2001; Gorman et al., 2008), element transport properties of metamorphic rocks (Skora et al., 2006; Konrad-Schmolke et al., 2008b), the prediction of compositional trends in arc melts (Hebert et al. 2009; Nagel et al., 2012) as well as quantification of reactive fluid flow during metamorphism (Beinlich et al., 2010).

1.2. Geochemical trace element modeling

Trace elements (elements that are present at concentrations of less than 0.1 wt.%) commonly substitute for major elements in rock-forming minerals. They have a negligible influence on the outcome of a particular process, but instead are passive recorders of the processes that the system has experienced (e.g., Blundy and Wood, 2003). The distinct geochemical behavior of trace elements, which can be described by mathematical models, makes them particularly useful tracers. Depending on the process, trace elements behave in different, but predictable ways, which allows us to determine which processes have operated in a certain situation or setting.

The low concentrations of trace elements cause them to be sufficiently diluted to follow simple relationships between composition and activity. For a wide range of trace element concentrations, Henry's Law applies, stating that the activity of a trace element is directly proportional to its composition:

$$a_i^A = h_i^A X_i^A,$$

where a_i^A is the activity of the trace element in phase A, h_i^A is Henry's Law constant (a proportionality constant or activity coefficient), and X_i^A is the composition of phase A. Commonly, the equilibrium distribution of trace elements between two phases is described by a distribution coefficient (or partition coefficient) (see White, 2013, for details). In

geochemical applications, the Nernst partition coefficient (D) is used, which defines D as the ratio of the concentrations (c) of an element i between two phases A and B:

$$D_i^{A/B} = \frac{c_i^A}{c_i^B}$$

Although D values are known to depend on temperature, pressure, and the compositions of the phases involved, P and T independent distribution coefficients are commonly used in magmatic and metamorphic petrology. This simplification is partly due to the limited pressure dependence of many partition coefficients under lithospheric conditions (Taura et al. 1998) and partly due to the lack of experimental data.

Quantitative models using trace elements were first applied in studies about the petrogenesis of igneous rocks. Gast (1968) and Shaw (1970) developed models for partial melting and fractional crystallization, in which they used concentrations of trace elements in liquid and solid phases in relation to the degree of partial melting of a rock and the degree of fractional crystallization, respectively. Later, assimilation of country rocks, combined assimilation – fractional crystallization processes, magma recharge, source rock heterogeneities and melt-rock reactions were all investigated using trace elements (O'Hara, 1977; De Paolo, 1981; Kelemen et al., 1992; McKenzie and O'Nions, 1991; Weaver, 1991). In recent years, trace element models are combined with thermodynamic constraints to simulate the evolution of magmatic systems that simultaneously undergo a combination of fractional crystallization, recharge and assimilation processes (EC-χAFC; Bohrson and Spera, 2001, 2007).

Trace elements are also important petrogenetic tracers for the genesis of metamorphic rocks. Whole rock trace element concentrations are frequently used for the determination of protolith compositions and pre-metamorphic alteration processes (Pearce 2008; Altenberger et al., 2008; Bebout, 2007; Becker et al., 2000; Halama et al., 2013; John et al., 2010; van der Straaten et al., 2012) and the quantification of fluid infiltration and element transport (Nabelek 1987; Ague, 2003, 2011; John et al., 2004; Beinlich et al., 2010). Many experimental studies have focused on the partitioning of trace elements between solid and liquid phases during subduction (Kessel et al., 2005; Ayers and Eggler, 1995; Brenan et al., 1995), and these data were applied in numerous investigations about fluid-rock interaction during metamorphism (Bau, 1991; Brunsmann et al., 2001; Breeding et al., 2004; Beinlich et al., 2010). In metamorphic rocks, several phases of metamorphism may be recorded, and partial overprinting during metasomatism and/or retrogression may cause additional

206 complexities. Therefore, *in situ* measurements that help to trace specific reactions and discern
207 different episodes of equilibration are often crucial.
208 Significant advances in modeling were achieved by the combination of thermodynamically
209 constrained equilibrium assemblage calculations with trace element fractionation models
210 between fluid/melt and residual phases. With this approach, specific features in the trace
211 element geochemistry of subduction-related rocks were successfully reproduced. Nagel et al.
212 (2012) combined the calculation of equilibrium assemblages in partially molten, mafic rocks
213 with subsequent modeling of trace element fractionation between melt and residual phases to
214 explain the formation of the Earth's oldest continental crust by melting arc tholeiites within a
215 tectonically thickened mafic island-arc crust (Fig. 1a). Hebert et al. (2009) investigated slab
216 fluid source lithologies and melt transport regimes in subduction zones using the GyPSM-S
217 (Geodynamic and Petrological Synthesis Model for Subduction) modeling scheme, which
218 couples a petrological with a thermal model to describe processes occurring in the supra-
219 subduction zone (SSZ) mantle wedge, supplemented with models for trace element
220 partitioning in the fluid phase and melt transport regimes. They interpreted geochemical
221 characteristics of across-arc and along-arc lavas in relation to distinct shallow and deep slab
222 fluid sources and found that melt migration through the mantle wedge preserves spatial
223 distinctions among melts initiated in different areas of the wedge (Hebert et al., 2009).
224 Focusing on the distribution of fluids in the mantle adjacent to a subducting slab, Hebert and
225 Montési (2013) modeled fluid transport and mantle hydration related to deep dehydration
226 reactions in subducted serpentinized mantle and effects on hydration of the transition zone.
227 Kimura et al. (2009) developed the Arc Basalt Simulator (ABS) modeling scheme to predict
228 the composition of primitive arc magmas (Fig. 1b). This simulation scheme initially included
229 slab dehydration and fluid-fluxed mantle melting and was subsequently modified to
230 incorporate slab melting and melt-fluxed mantle melting (Kimura et al., 2010) and, most
231 recently, separate P-T paths for distinct slab layers, yielding more liquid-solid interaction
232 within the 1-D vertical column (Kimura et al., 2014). Application of the ABS models
233 produced successful predictions of incompatible element and Sr-Nd-Pb isotopic compositions
234 of distinct primitive magmas from the volcanic front and the rear-arc of the Izu arc (Kimura et
235 al., 2010).
236
237 *1.3. Boron and boron stable isotopes as tracers of fluid-rock interaction*

238 One of the key aspects in metamorphic petrology is to trace and quantify liquid phases
239 percolating through solid rocks. Liquid phases, such as aqueous fluids or melts, are the major

transport agents in the solid Earth and thus quantification of the fluxes of liquid phases enables tracing of the mass transfer in the solid Earth. In contrast to a melt phase, which might crystallize *in situ* and can then be directly investigated, fluids can only be passively trapped as inclusions in solid phases and in most cases have left the rock at the time of investigation. Thus, indirect geochemical evidence for the presence of a fluid interacting with the host rock must be considered. Ideally, such indirect geochemical proxies for fluid-rock interaction are among the fluid mobile elements (FME), have quick equilibration times and small equilibration volumes. Subsequent to fluid-rock interaction, the geochemical proxy must be stable and not prone to later, e.g. diffusional, re-equilibration. Furthermore, the proxy must be present in major phases in measurable quantities. Elements often used for this purpose are Li, B, N, Cl, As, Rb, Sb, Cs, Ba as well as Pb and U (see Ryan and Chauvel 2013).

Boron is particularly useful for the investigation of fluid-rock interaction processes and dehydration because it is present in measurable quantities in several major mineral phases (white mica, tourmaline, amphibole, serpentine) as well as in hydrous fluids and its concentration is typically low enough to make it sensitive to fast equilibration at small fluid amounts. In most rock-forming minerals, including white mica, B substitutes for silica and occupies the tetrahedral position (Sanchez-Valle et al., 2005). If B diffuses similarly slow as Si, B concentrations are difficult to exchange after crystallization (Hervig et al., 2002), a prerequisite to preserve relevant information over geologic time scales. Furthermore, information from boron as fluid-mobile trace element can be combined with the isotopic information from B stable isotopes (e.g., Simon et al., 2006).

The observation of variations in the atomic weight of boron in minerals, made by Briscoe and Robinson (1925), was crucial for the recognition that physiochemical processes can cause isotopic fractionation of light elements in natural substances. It was therefore proposed that geologically relevant processes, including melting, crystallization, solution and volatilization, would cause isotopic variations in nature (Briscoe and Robinson, 1925), leading the way for the widespread application of stable isotopes as tracers (Sharp, 2007). The value of the various stable isotope systems is based on the fact that distinct stable isotope signatures occur in different reservoirs, so that they can be used to trace the origin of rocks and fluids.

Boron has two stable isotopes, ^{10}B and ^{11}B, with relative abundances of 19.8% and 80.2%, respectively. The large B isotopic variation in natural substances of almost 100‰ (Fig. 2; Deyhle and Kopf, 2005) is dominantly due to differences in coordination between tetrahedral

$B(OH)_4^-$ and trigonal $B(OH)_3$. Moreover, the B isotopic composition is influenced by temperature-dependent equilibrium fractionation between solid and fluid phases (Peacock and Hervig 1999; Hervig et al., 2002; Wunder et al., 2005) and it is also sensitive to changes in the pH value (Deyhle and Kopf, 2005). Boron preferentially partitions into the fluid phase (Brenan et al., 1998) with a concomitant enrichment of the heavy isotope ^{11}B relative to ^{10}B. The most striking example of coupled trends of elemental and isotopic variations occurs in arc lavas, where systematic across-arc trends of decreasing and isotopically lighter B with increasing slab depths (Fig. 2; Ishikawa and Nakamura, 1994; Ishikawa et al., 2001; Moriguti et al., 2004) are attributed to contributions from a slab-derived agent that successively reflects increasing degrees of slab dehydration and decreasing slab-to-arc element transfer (Bebout et al., 1999; Rosner et al., 2003; Marschall et al., 2007). In addition, several studies have emphasized the role of serpentinized mantle rocks, both in the supra-subduction zone wedge and in the subducting slab mantle, for boron cycling in subduction zones (Tonarini et al., 2007, 2011; Benton et al., 2001; Hattori and Guillot, 2003; Savov et al., 2007). Evidence for the sensitivity of the B system for fluid-rock interaction is provided by zoning patterns in various metamorphic minerals (white mica, amphibole, tourmaline), which retain information about the compositional evolution of metasomatic fluids through the metamorphic history (Bebout and Nakamura, 2003; Marschall et al., 2009; Konrad-Schmolke et al., 2011b; Halama et al., 2014).

In the following sections we will show two examples of combined thermodynamic-geochemical models that focus on the mass transfer in subduction zones at different spatial scales (Fig. 3). The first model simulates fluid-rock interaction at grain-scale and investigates the effect of fluid percolation on B concentrations and B isotopic compositions in partially overprinted phengites. In the second example, fluid release from a subducted slab, the associated transport of B and variations in B concentrations and isotopic compositions in liberated fluids and residual rocks are modeled. We compare the results of both examples with observations in natural minerals and rocks in order to quantify fluid fluxes and element cycling.

2. Example 1: Boron and boron isotopes in white mica during high-pressure fluid-rock interaction

2.1. Observations in natural samples

Fluid-induced metasomatic overprinting is a common feature in many metamorphic terranes

(e.g., Sorensen and Grossman, 1989; John et al., 2004; Bebout, 2007; Beinlich et al., 2010; Halama et al., 2011). Partial re-equilibration of metamorphic rocks, immensely important to trace the rocks' metamorphic evolution, results in whole rock geochemical and isotopic variations and in compositional changes in individual metamorphic minerals (Spear and Selverstone 1983; Thompson and England 1984; Yardley et al., 1991; Kohn 2003; Habler et al., 2007; Konrad-Schmolke et al., 2011a,b; Pearce and Wheeler, 2010; Goncalves et al., 2012). Since white mica is ubiquitous in metamorphic rocks of both igneous and sedimentary origin and stable over a wide P-T range, especially in high pressure rocks (Domanik and Holloway, 1996; Hermann and Spandler, 2008), it is well suited to investigate fluid-rock interaction processes during metamorphism. Chemical variations in white mica depend on P-T conditions, bulk rock composition and syn-kinematic mass transfer and fluid conditions (Velde, 1965; Massonne and Schreyer, 1987; Guidotti et al., 1994; Goncalves et al., 2012). Diffusion-controlled exchange reactions in white mica have relatively high closure temperatures below which major element exchange is effectively impossible, so that preserved chemical variations predominantly reflect deformation and recrystallization controlled equilibria (Dempster, 1992). Potassic white mica is also amenable to age dating using both the $^{40}Ar/^{39}Ar$ and Rb-Sr methods and hence provides a means to directly link age information to the metamorphic evolution of a rock (Di Vincenzo et al., 2001; Glodny et al., 2002; Bröcker et al., 2013; Halama et al., 2014; Warren et al., 2011, 2012). White mica is also an important carrier of fluid-mobile trace elements including B, lithium (Li) and the large ion lithophile elements (LILE; K, Cs, Rb, Ba, Sr; Bebout et al., 1999, 2007, 2013; Konrad-Schmolke et al. 2011b; Hermann and Rubatto, 2009). Boron is concentrated in white mica (phengite and paragonite), compared to all other major phases, except tourmaline (Domanik et al., 1993; Marschall et al., 2006). Hence, white mica dominates the B budget in most tourmaline-free rocks and its B isotopic composition can be considered as representative of the bulk rock (Peacock and Hervig, 1999). During subduction, the presence of white mica critically determines retention and release of B as well as the B isotopic composition of released fluids (Marschall et al., 2007). Therefore, B elemental and isotopic changes in white mica are ideally suited to trace compositional changes due to fluid-mediated metasomatism. However, B isotope data in white mica are still relatively rare (Peacock and Hervig, 1999; Pabst et al., 2012; Angiboust et al., 2014) as many B isotope studies concentrated on tourmaline (Bebout and Nakamura, 2003; Trumbull et al., 2008, 2009; Marschall et al., 2009).

In this example, we present a detailed study of high-pressure metamorphosed felsic rocks of the Western Alpine Sesia Zone (SZ) that were exhumed from mantle depths on top of a

dehydrating subducted oceanic plate where they directly interacted with percolating fluids at blueschist-facies conditions. A sampling profile across a deformation gradient around a major blueschist-facies shear zone showed several remarkable compositional features in texturally different phengite grains and domains (Konrad-Schmolke et al., 2011a,b, Halama et al., 2014).

2.1.1. Phengite chemistry in the Sesia Zone samples

Fluid infiltration in weakly deformed rocks modified primary phengite (3.3 - 3.5 Si p.f.u., X_{Mg} = 0.6 - 0.7) compositionally along fluid pathways (Fig. 4a and b). Fluid-induced retrograde major element equilibration of phengite involves a major decrease in X_{Mg} and is visible in high contrast BSE images, which show darker-colored cores surrounded by brighter zones that are concentrated at the tips and grain boundaries, around inclusions and in deformed parts (Fig. 4a). The BSE images show one, in some places two different replacement zones as well as areas with diffuse transitions, but oscillatory zoning is missing.

Phengite cores in weakly deformed samples have variable $\delta^{11}B$ values (-18 to -10‰) that were interpreted to reflect the lack of km scale B homogenization during HP crystallization (Fig. 4c). Corresponding overprinted phengite rims have lower B abundances but overlapping $\delta^{11}B$ values (-15 to -9‰), thought to reflect predominantly internal redistribution of B and internal buffering of the B isotopic compositions during recrystallization of the rims (Halama et al., 2014). In contrast, fine-grained mylonitic phengites are compositionally homogeneous in their major and trace element concentrations. X_{Mg} and Si p.f.u. in the syn-kinematic phengites correspond to the values observed in the overprinted phengite rims of the weakly deformed samples. Boron is almost completely removed in the mylonitic phengites (1-10 µg/g). The boron isotopic compositions in the mylonitic phengites are significantly heavier than in those from the weakly deformed samples, indicating an external control by a high-$\delta^{11}B$ fluid ($\delta^{11}B$ = +7±4‰). The compositional trend leads from relict cores via overprinted rims towards the mylonitic phengites (Fig. 4c). Based on estimates of the time-integrated fluid fluxes, which are more than one order of magnitude higher in the mylonites (Konrad-Schmolke et al. 2011b), the B removal was related to fluid-induced phengite recrystallization.

The sample profile, with presumably unmodified peak P-T phengite cores in weakly deformed samples, a partial metasomatic overprint represented by the phengite rims, and a strong deformation coupled to intense fluid-rock interaction in the mylonitic phengite provide the conceptual basis for fluid-rock interaction modeling along a distnct P-T path (Fig. 5). In

371 particular, we focus on the apparent paradox of lower B contents at similar $\delta^{11}B$ values in the
372 overprinted areas. Moreover, we want to evaluate to which degree the accurate determination
373 of the two parameters [B] and $\delta^{11}B$ allows a quantification of fluid amounts that have
374 interacted with the rock.

375 *2.2. Thermodynamic-geochemical modeling of B concentrations and isotopic compositions in*
376 *phengite*

377 The boundary conditions for the thermodynamic model that has been performed with the
378 THERIAK algorithm (de Capitani and Brown 1987) in the NCKFMASH chemical system
379 comprise the following assumptions: Along the prograde P-T path, the samples underwent
380 fractional garnet crystallization, indicated by large, compositionally zoned garnet
381 porphyroblasts in the natural samples, and water fractionation due to devolatilization reactions
382 (Konrad-Schmolke et al., 2011a). Thus, calculation of the effective bulk rock composition
383 (EBC) at the start of the retrograde P-T trajectory must consider a prograde segment
384 accounting for the element fractionation processes. Along the retrograde P-T path, from 2.0
385 GPa and 575°C to 1.1 GPa and 500°C (Fig. 5), a fluid influx event occurs at about 1.35 GPa
386 and 550°C, which causes water re-saturation in the affected areas of our samples.

387 The mineralogical evolution of the samples in the P-T-X-space can be displayed with two
388 compositionally constrained P-T equilibrium assemblage diagrams (P-T pseudosections) (Fig.
389 5a) and a P-X diagram (Fig. 5b). Fractional garnet crystallization and water fractionation
390 along the prograde P-T path continuously modified the EBC. At peak conditions (left
391 diagrams in Fig. 5a), the rock is water-saturated and becomes water under-saturated along the
392 first segment of the retrograde P-T trajectory. The diagram calculated for the EBC at peak
393 conditions shows that there is no significant change in the phase assemblage
394 (pg+gln+cpx+phng+qtz) along the retrogade path until fluid influx at 1.35 GPa and 550°C.
395 The fluid influx causes water re-saturation of the EBC and changing phase relations (right
396 diagrams in Fig. 5a) that are then applicable for the second part of the retrograde P-T
397 trajectory. The P-H_2O diagram (Fig. 5b) highlights the compositional plane in the P-T-X
398 space together with the retrograde P-X trajectory of our samples (red arrow). Below the water
399 saturation line (bold blue) X_{Mg} in phengite strongly depends on the H_2O content indicated by
400 the sub-vertical X_{Mg} isopleths. The compositional correlation between H_2O content and X_{Mg}
401 in phengite is reflected in the fluid-induced overprinting zones in the mica grains of the
402 natural samples (Fig. 4a). The modeled phase relations and phengite compositions along the
403 retrograde P-T trajectory demonstrate that the fluid influx causes drastic changes in both

modal mineralogy and phase chemistry (Fig. 6).

Phengite amount decreases by about 10 wt.%, whereas the abundances of glaucophane and paragonite increase. Omphacite is no longer stable and epidote joins the stable phase assemblage. In phengite, the model indicates a slight decrease in Si_T due to the fluid influx, unrelated to the continuous pressure decrease (Fig. 6a). The negative correlation between decreasing celadonite (X_{Cel}) and increasing ferroceladonite (X_{Fcel}) components reflects the sudden increase in X_{Fe} in the overprinted zones. These modal and chemical phase changes reflect the blueschist-facies overprint as observed in the shear zone (Konrad-Schmolke et al., 2011a).

Boron concentrations [B] and isotopic compositions ($\delta^{11}B$) of phengite (phng) are modeled along the retrograde P-T path. Boron distribution among fluid and stable mineral phases is calculated using partitioning data of Brenan et al. (1998) and Marschall et al. (2007). Specifically, the $D^{fluid\text{-}phng}$ value was derived from $D^{cpx\text{-}fluid}$ (Brenan et al., 1998) and $D^{cpx\text{-}phng}$ (Marschall et al., 2007). Experimentally determined B isotope fractionation data were taken from Wunder et al. (2005). Initial values for [B] and $\delta^{11}B$ in the host rock are chosen to reflect the composition of the phengite cores, whereas [B] and $\delta^{11}B$ in the infiltrating fluid (27 µg/g and +7‰) were calculated assuming chemical equilibrium with the mylonites in the shear zone. A detailed modeling description together with a software package including the Gibbs energy minimization algorithm THERIAK (de Capitani and Brown 1987) together with a MatLab® script for B and $\delta^{11}B$ calculations are given in the electronic supplementary material.

2.3. Geochemical model results

The modeling of [B] and $\delta^{11}B$ in phengite relates the amount of water that percolated through the rock to the structural and textural characteristics of phengite in the natural samples (Fig. 7). High-pressure conditions at P > 1.35 GPa – before the fluid influx – are represented by relict, unmodified phengite cores. Predominantly internal B redistribution and low amounts of water influx are mirrored in the overprinted rims, whereas high amounts of water reflect conditions in the shear zone. The model shows that with increasing water flux, [B] in phengite decreases (Fig. 7a) due to the preferential partitioning of B into the fluid. The redistribution of B is quite efficient even at low amounts of water influx, so that a constant [B] value is reached after only 0.5 wt.% accumulated water influx. The changes in $\delta^{11}B$, caused by the preferential partitioning of ^{11}B into the fluid, are more sluggish (Fig. 7b). At very low water

436 fluxes the isotopic composition of white mica is even driven towards slightly lower $\delta^{11}B$
437 values, a trend that is reversed after ~0.1 wt% water influx. About 1 wt.% H_2O is required
438 before a constant $\delta^{11}B$ value is reached in the model.

439 When distinct amounts of water influx (0, 0.09 and 1.5 wt.%) for the given P-T path are
440 compared, the rapid chemical and isotopic changes of the predicted B equilibrium
441 concentrations and isotope compositions become even more apparent (Fig. 7c,d). If no water
442 is added, representing a completely internal redistribution of boron, the model predicts a small
443 increase of [B] in phengite associated with unchanged $\delta^{11}B$ compared to the pre-influx values.
444 Low water influx (0.09 wt.%) causes a 20% decrease in [B], consistent with B concentrations
445 measured in the overprinted rims. The modeled $\delta^{11}B$ in phengite resulting from fluid-rock
446 interaction at these low fluid fluxes is much less affected and changes by less than 1‰. The
447 modeled B isotopic variation is within analytical uncertainty and natural inhomogeneity
448 between different samples. Indeed, most samples do not show B isotopic differences between
449 relict cores and rims, albeit a tendency towards higher $\delta^{11}B$ values is recognizable for some.
450 High fluid influx (1.5 wt.% accumulated water flux) results in an 80% decrease in [B],
451 whereas $\delta^{11}B$ increases toward the equilibrium value determined by the external fluid. Again,
452 both features agree well with the field-based observations in the SZ.

453 The interplay of the two parameters [B] and $\delta^{11}B$ during progressive fluid influx allows a
454 quantification of the amounts of fluid absorbed by the rocks. The evolution of [B] and $\delta^{11}B$ in
455 the percolating fluid are decoupled at low amounts of H_2O. Whereas removal of B from the
456 interacting host rock leads to a continuous decrease in [B] immediately after infiltration of the
457 first increment of fluid, $\delta^{11}B$ initially slightly decreases. With increasing fluid amount, the
458 trend in $\delta^{11}B$ reverses. In our example, the amount of water in the weakly deformed samples
459 is limited to a maximum of ~0.25 wt.%. In the mylonites, at least 0.75 wt.% water must have
460 been percolating through the rock to explain the changes in both [B] and $\delta^{11}B$. One of these
461 parameters alone would not suffice to quantify fluid amounts.

462 Decreasing B concentrations in minerals and rocks are commonly attributed to dehydration
463 reactions as evident in figures 2 and 8 whereas in the chosen example decreasing B
464 concentrations in phengite are the result of the fluid infiltration and fluid-rock interaction
465 leading to a B redistribution and precipitation of phengite material with lower B
466 concentration. In contrast to dehydration that is associated with decreasing $\delta^{11}B$ values, fluid-
467 rock interaction in the investigated samples causes an increase in $\delta^{11}B$ in the affected phengite
468 grains, which demonstrates that only the combination of the two parameters [B] and $\delta^{11}B$

allows distinction between the two contrasting processes.

It is notable that in our samples overprinted phengite areas are visible in BSE images due to their significantly higher Fe concentrations and B measurements can be correlated with these zones. To evaluate whether the B compositional and isotopic zoning in the investigated phengites fully correlates with the major element zonation, qualitative mappings of single grains are necessary. Such mappings of trace element compositional variations in metamorphic minerals are crucial to increase our knowledge about the fluid-rock interaction and associated processes in metamorphic phases (e.g., Papst et al., 2011; Valle et al., 2011). At present, relatively large analytical uncertainties for B isotope compositions measured in natural phengite (2s uncertainty = 1-5 ‰) make it difficult to detect intra-grain variations in samples with low B concentrations and small grain sizes (Aggarwal and Palmer, 1995; Jacob, 2006; Rosner et al., 2008), but in contrast to B-rich phases, such as tourmaline, white mica has the advantage that it is a rock-forming phase in many metamorphic rocks and its compositional variations can easily linked with its metamorphic evolution (e.g., Massonne and Schreyer 1987). Our example shows the capacity of B concentrations and the isotopic composition of B in phengite to record fluid influx and fluid-rock interaction in metamorphic rocks (e.g., Angiboust et al., 2014). Qualitatively, the results of this example demonstrate that the effects of fluid-rock interaction during fluid percolation on the trace element transport may be profound and need to be considered in large-scale subduction zone models, which will be delineated below.

3. Example 2: Boron release in subduction zones

3.1. Observations in natural samples

Subduction of hydrated oceanic lithosphere is the main process that allows element transfer from the Earth's surface to the deeper mantle. Devolatilization of the subducted slab leads to partitioning of elements into the upward migrating fluid and subducting solid phases. Whereas the former are recycled into the upper plate or the atmosphere, the latter are deeply subducted and assimilated into the deep mantle (Elliott et al., 2004; Peacock and Hervig, 1999; Hofmann, 1997; Hacker, 2008). Knowledge about and quantification of this element partitioning is crucial for the understanding of global scale element distribution between crust, mantle and atmosphere (e.g., Connolly, 2005; Kerrick and Connolly, 2001; Spandler and Pirard 2013). As we have no direct access to the subducting rocks, elemental and isotopic signatures in arc volcanic rocks are interpreted in terms of processes occurring in the

downgoing slab (Pearce and Peate, 1995), although the extent to which slab contributions control geochemical characteristics of arc magmas is disputed (Elliott, 2003). However, there are several examples where across-arc geochemical variations in arc lavas appear to reflect changes in the subducting slab as a function of depth (Fig. 2), which in turn control slab-to-arc mass transfer (Ishikawa and Nakamura, 1994; Ryan et al., 1995, 1996; Moriguti and Nakamura, 1998). Geochemical reservoirs in the slab that potentially leave their imprints in arc volcanic signatures include all lithological layers of the subducting lithosphere: sediments, igneous oceanic crust and the hydrated slab mantle (Ryan et al., 1995; Plank and Langmuir, 1993; Morris et al., 1990; John et al., 2004; Herms et al., 2012). If seawater is able to infiltrate the upper oceanic mantle (Ranero et al., 2003; Ranero and Sallarès, 2004; Garth and Rietbrock, 2014), serpentinites formed by this process can theoretically absorb up to 13 wt% of water and may therefore be effective carriers of water (Schmidt and Poli 1998; Rüpke et al., 2004; Hacker, 2008) and certain fluid-mobile elements (FME) to sub-arc depths (Ulmer and Trommsdorff, 1995; Scambelluri et al., 2001; Hattori and Guillot, 2003). Additionally, the supra subduction zone (SSZ) wedge mantle, which is hydrated by fluids liberated from the subducted slab, may also be an important reservoir of water and trace elements delivered to greater depth (Tatsumi, 1986; Hyndman and Peacock, 2003; Straub and Layne, 2002; Hattori and Guillot, 2003; Kawamoto et al., 2013), although both water and FME are originally derived from the slab itself. If SSZ mantle is dragged down along the slab-wedge interface towards sub-arc depth (Savov et al., 2005, 2007), and if temperatures remain cold enough so that relevant dehydration reactions are delayed until these depths are reached (Grove et al., 2009; Till et al., 2012), geochemical signals from SSZ mantle-derived fluids may be incorporated into arc melt sources. A thermodynamic-geochemical model reflecting fluid liberation and reactive fluid flow (Zack and John 2007) in subduction zones must incorporate fluid production and fluid-rock interaction in all of the above-mentioned reservoirs.

Regarding the use of B as tracer for subduction zone processes, Ryan and Langmuir (1993) first noted that B is a useful proxy in across-arc studies by observing systematically lower B contents in arcs where volcanoes sample deeper portions of the slab. As B concentrations in dry mantle rocks are extremely low (<1 µg/g), B is flushed through the SSZ mantle wedge without significant modification of the B slab signal during fluid ascent (Ryan and Langmuir, 1993). Compared to the mantle wedge, B is concentrated in several slab lithologies, including subducted sediment (Ishikawa and Nakamura, 1993), altered oceanic crust (AOC) (Spivack and Edmond, 1987; Yamaoka et al., 2012) and serpentinized mantle rocks (Benton et al., 2001; Boschi et al., 2008; Vils et al., 2009; Scambelluri et al. 2004). Arc lavas are generally

535 enriched in B, as shown by elevated B/Nb and B/Be ratios compared to oceanic basalts (Fig.
536 2a). The B/Nb ratio is used as tracer of B enrichment because B/Nb is considered as
537 unfractionated during partial melting based on similarity in mineral-melt partition coefficients
538 (Brenan et al., 1998). Arc lavas are also relatively enriched in ^{11}B (Fig. 2b), suggesting fluid-
539 mediated slab-to-arc B transfer via a B-rich, high-$\delta^{11}B$ slab fluid (Scambelluri and Tonarini,
540 2012). In many cases, the B isotopic compositions systematically vary with B enrichment as
541 higher B/Nb ratios are coupled to higher $\delta^{11}B$ values (Fig. 2a; Spandler and Pirard, 2013).
542 Consequently, across-arc trends with increasingly lower B concentrations and isotopically
543 lighter compositions with increasing slab-surface depths, as observed in many subduction
544 zones (Fig. 8b; Ishikawa and Nakamura, 1994; Ishikawa et al., 2001; Ishikawa and Tera,
545 1999; Rosner et al., 2003), are interpreted to directly reflect increasing degrees of slab
546 dehydration and decreasing slab-to-arc element transfer. However, several subduction zones
547 show unusually high $\delta^{11}B$ and B/Nb values or reversals in the across-arc trends of these
548 values (Moriguti et al., 2004; Ishikawa et al., 2001; Tonarini et al., 2001), but the reasons for
549 these exceptions are still debated. Among the most interesting of the deviating examples are
550 the South Sandwich Islands (SSI) arc and the Kamchatka subduction zone. In the SSI arc,
551 anomalously high $\delta^{11}B$ and B/Nb are observed throughout the entire volcanic arc and
552 interpreted to reflect dehydration of the SSZ wedge mantle (Tonarini et al., 2011). Across the
553 Kamchatka peninsula, arc volcanic rocks from three successive volcanic chains yield a
554 complex $\delta^{11}B$ and B/Nb pattern (Fig. 2; Ishikawa et al., 2001), the reason for this complexity
555 being unclear so far, but possibly related to dehydration of subducted slab mantle. Slab
556 mantle dehydration is difficult to detect in arc volcanic rocks by geochemical means because
557 ultramafic rocks are typically poor in many trace elements. Arsenic, antimony and boron are
558 among the few elements characteristic for serpentinites and geochemical trends of these
559 elements (Spandler and Pirard, 2013) as well as the isotopic composition of boron in arc lavas
560 are interpreted to reflect serpentinite dehydration (Tonarini et al., 2011). However,
561 geochemical models alone cannot discriminate between dehydration of upper- and lower-plate
562 serpentinites. If and to which degree slab mantle dehydration influences $\delta^{11}B$ and B/Nb in
563 across-arc profiles can be tested with a combined thermodynamic-geochemical model, which
564 utilizes boron and its isotopic composition to model slab fluid release and fluid rock
565 interaction in the downgoing slab and the mantle wedge.

566 *3.2. Modeling B concentrations and isotopic compositions in a subduction zone*

567 Marschall et al. (2007) modeled B concentrations in subducting rocks and released fluids

568 during subduction by combining the B distribution among the minerals present with
569 temperature-dependent fractionation of B isotopes, corroborating the proposed continuous
570 decrease in B and $\delta^{11}B$ in both residual rocks and released fluids (Fig. 8). These one-
571 dimensional models predict that white mica plays a crucial role in the B geochemical cycling.
572 The more white mica is present in the rock, the more B is retained in the slab down to subarc
573 depths and beyond, and the more positive are the $\delta^{11}B$ values of the released fluids (Marschall
574 et al., 2007). Based on this pioneering work, our models additionally incorporate a
575 sedimentary layer, a layer of oceanic mantle in the subducting slab as well as a SSZ mantle
576 wedge layer (Fig. 9a), thus expanding the model to a second dimension (cf. Connolly, 2005;
577 Rüpke et al., 2006). Moreover, interaction between the liberated water and the wall rock
578 during the ascent of the fluid phase is taken into account because fluid-rock interaction within
579 the slab, at the slab-wedge interface (Marschall et al., 2006) and in the overlying mantle
580 wedge can lead to significant modifications of both percolating fluid and the affected wall
581 rock with respect to [B] and $\delta^{11}B$. In our model, a thermal subduction zone pattern (Fig. 9a) of
582 the Kamchatka subduction zone derived from finite element thermomechanical modeling
583 (Manea and Manea, 2007) is used as pressure-temperature input for a Gibbs energy
584 minimization algorithm (PERPLE_X; Connolly 2005) that simulates the passing of a vertical
585 rock column within the subducted slab through the steady state thermal pattern. The thermal
586 pattern is modeled with a finite element grid extending from 25 km seaward of the
587 Kamchatkan trench up to 600 km landward of it. The numerical scheme solves a 2D Navier-
588 Stokes equation and a 2D steady state heat transfer equation. Shape and dip of the subducting
589 plate beneath the active arc are constrained by the earthquake hypocenter distribution (see
590 Manea and Manea 2007 for further details). Phase relations within the rock column that
591 consists of a SSZ mantle wedge layer (10 km; Primitive Upper Mantle from Workman and
592 Hart, 2005), a sediment pile (625 m; GLOSS from Plank and Langmuir, 1998), igneous
593 basaltic crust (6.4 km; N-MORB from Workman and Hart, 2005) and a variably hydrated slab
594 mantle (18.5 km; Depleted Mantle from Workman and Hart, 2005) are calculated with a
595 resolution of 250 x 250m. A more detailed description of the model and input parameters
596 together with a MatLab® script can be found in the electronic supplement. Water liberated by
597 dehydration reactions is transported vertically upward, equilibrating at every calculated
598 increment within the column, thus reflecting a high ratio of fluid/slab migration velocity. The
599 modeled phase relations at every calculated increment are used for a coefficient-based mass-
600 balanced B distribution (Brenan et al., 1998) and a temperature-dependent fluid-solid B
601 isotope fractionation (Fig. 9b; Wunder et al., 2005). The model simulates fluid release, fluid

migration, fluid-rock interaction and boron transport in a subducted slab and the overlying mantle wedge. Comparison of modeled and observed B concentrations and isotopic patterns help to constrain initial hydration of the slab and the dehydration behavior of wedge mantle and slab during subduction.

3.3. Model results

The dehydration model of the subduction zone shows that water release from the slab is controlled by thermally induced breakdown of the hydrous minerals brucite, antigorite, chlorite and lawsonite (Figs. 10 and 11). In case of a dry slab mantle dehydration occurs up to 250 km slab surface depth and is characterized by a continuous crustal signal and superimposed dehydration spikes resulting from discontinuous wedge mantle and slab crust dehydration (Fig. 11a). Breakdown of brucite and antigorite with minor contributions from chlorite and amphibole in the SSZ wedge mantle dominates water release in the fore-arc region. In the sub-arc region, water is delivered by continuous chlorite dehydration from the crust and the chlorite-out reaction in the SSZ mantle wedge that causes a characteristic dehydration peak at ~130 km slab surface depth. As predicted by the models of Marschall et al. (2007), continuous dehydration of the slab leads to a drastic decrease of the B concentrations (Fig. 11b) as well as to decreasing $\delta^{11}B$ values (Fig. 11c) in the residual rocks. However, depending on the depth within the slab crust the B concentrations in different rocks from the same layer can have significantly different values and a concentration gradient within the slab is maintained up to 200 km slab surface depth. This circumstance is the result of the interplay between the predominantly temperature-controlled dehydration pattern that is skewed relative to the surfaces of the lithological layers and the leaching effect resulting from fluid percolation within the slab. The effect of fluid-rock interaction on the subducted rocks is also clearly visible in the $\delta^{11}B$ values at different positions within the slab. Differences in the $\delta^{11}B$ values between the slab surface and in the SSZ mantle wedge subsequent to fluid-rock interaction can be as large as 10‰ in shallower regions and are about 5‰ at greater slab surface depths. These results show the need for two or three-dimensional models regarding the prediction of B concentrations and $\delta^{11}B$ values in subduction-related fluids and rocks.

Utilizing the same model setup, the effect on [B] and $\delta^{11}B$ values in the fluids released by slab mantle dehydration can be studied. In contrast to the preceding model, the slab mantle is now initially hydrated to a depth of 15 km perpendicular to the slab mantle surface. This is the maximum depth to which hydrous phases are thermodynamically stable at the beginning of the model run. The pseudosection (Fig. 10b) shows that chlorite and serpentine are the stable

hydrous phases in the slab mantle up to 175 km slab surface depth. Depending on the thermal pattern within the slab there is an overlap of the stability fields of antigorite and phase A, enabling the transfer of H_2O into the deeper mantle beyond sub-arc depths (cf. Hacker, 2008). As there is no water release from the slab mantle at slab surface depths less than 175 km, the dehydration pattern of the hydrated slab mantle up to this depth is the same as in the dry slab mantle case (Fig. 12a). Water released by chlorite breakdown in the slab mantle is directly transferred into serpentine at slab depth of about 150 km. Subsequently, the antigorite breakdown reaction is the key factor regarding water release from the slab mantle (Fig. 12a). The antigorite-out reaction starts at the bottom of the hydrated slab mantle part at ~130 km slab surface depth. The liberated water migrates into the water-undersaturated overlying part of the slab mantle, where it is resorbed and dragged down until the thermal stability limit of antigorite is reached at ~175 km slab surface depth. The model shows that large amounts of water are liberated at the terminal antigorite-out reaction, causing a massive fluid flux into the overlying slab crust and wedge mantle. This dehydration burst is responsible for the second, most prominent peak superimposed on the crustal dehydration pattern (Fig. 12a). Beyond the antigorite-out reaction in the slab mantle, minor water release continues by lawsonite breakdown in the crustal part of the slab. Phengitic white mica remains stable in the crustal parts of the slab and does not significantly contribute to water release.

Based on the mass balanced boron distribution, the mass of boron (kg B/m^3 rock) released from the slab is calculated (Fig. 12b). These values show a drastic decrease across the profile down to ~170 km slab surface depth, followed by a characteristic and spike-like increase where antigorite dehydration takes place in the slab mantle. The continuous water release from SSZ wedge serpentinites and slab crust explains the strongly decreasing B supply with increasing slab depth because the fluid-mobile B is flushed out with the water. Thus, our model reproduces the decreasing B/Nb ratios observed in various across-arc trends that were attributed to continuous dehydration reactions in the oceanic crust (Ryan et al., 1995; Marschall et al., 2007). At the tip of the antigorite-out reaction in the slab mantle, the transfer of large amounts of boron into the hanging wall plate is predicted, causing B enrichment in arc melts generated there. In terms of B isotope composition, our model shows high $\delta^{11}B$ values in the fore-arc region, followed by a continuous linear decrease in $\delta^{11}B$ from ~110 to ~175 km slab surface depth and a distinct increase where the terminal antigorite-out reaction in the slab mantle is located (Fig. 12c). Initially, dehydration of sediments and SSZ wedge serpentinites releases extremely heavy boron into the fore-arc region, as observed in fore-arc slab fluids from serpentinite seamounts (Benton et al., 2001). Subsequently, dehydration of

669 the igneous oceanic crust exemplifies the continuous dehydration-induced ^{11}B depletion in the
670 residual rocks leading to a decreasing $\delta^{11}B$ trend in the released fluids (Marschall et al., 2007;
671 Rosner et al., 2003). This trend has not only been observed in Kamchatka, but also in the
672 Kurile (Ishikawa and Tera, 1997), West Pacific (Ishikawa and Nakamura, 1994) and Chile
673 (Rosner et al., 2003) subduction zones (Fig. 2). Finally, the high-B fluid released by antigorite
674 breakdown in the slab mantle directly transfers a high-$\delta^{11}B$ signature towards the surface due
675 to the high water flux and the finite capability of the crust to incorporate B. Continuing
676 dehydration of slab crust alone is not able to deliver any significant amounts of water or
677 boron at that depth. A major implication of our model is that the absolute $\delta^{11}B$ values
678 expected where antigorite breaks down depend on the hydration state of the slab mantle. In
679 the slab crust, refertilization leads to an additional decreasing $\delta^{11}B$ trend caused by the
680 lawsonite-out reaction between 200 and 250 km slab depth, although this trend is blurred at
681 the model surface by fluid-rock interaction.

682 If we assume unmodified transport of the B signal from the top of the model surface through
683 the upper part of the SSZ wedge mantle and the continental crust, the distinct [B] – $\delta^{11}B$
684 relationship of fluids derived from wedge mantle, crust and slab mantle may be used to
685 identify fluid source lithologies in arc lavas (Fig. 13). It is notable that the position of the slab
686 mantle dehydration is primarily dependent on the stability of antigorite. In our
687 thermodynamic model we use a binary Fe-Mg, Al-free solid solution model of antigorite,
688 which might underestimate the upper stability limit, as Al incorporation into antigorite can
689 result in an increase of the maximum stability in the order of 30°C (Padrón-Navarta et al.,
690 2013). Regarding the spatial scale of our model, together with the fact that Al solution into
691 antigorite has insignificant effects on the co-existing phase relations, we assume this
692 uncertainty to be of minor importance for our interpretation. As pointed out by Scambelluri
693 and Tonarini (2012), arc lavas with $\delta^{11}B$ greater than that of slab fluids require serpentinite as
694 source component. The relatively B-rich, high-$\delta^{11}B$ nature of the South Sandwich lavas (Fig.
695 2) was attributed to the influence of serpentinite-derived fluids from the mantle wedge
696 (Tonarini et al., 2011), in agreement with the characteristics of the modeled mantle wedge –
697 derived fluids. In contrast, slab-derived fluids are expected to have lower B contents. Fluids
698 derived from the slab crust trend toward negative $\delta^{11}B$ values, whereas those from the slab
699 mantle have positive $\delta^{11}B$ values (Fig. 13). For each individual subduction zone modeled,
700 thermal constraints and variations in the input parameters need to be taken into account when
701 evaluating the calculated values. Using the additional constraints of the location relative to the
702 trench and the depth to the slab, which are available for natural samples, the pattern modeled

here may serve as a useful guide in evaluating fluid sources. For the Kamchatka subduction zone model, the difference in $\delta^{11}B$ between fluids derived from slab crust compared to slab mantle is on average about 10‰, but importantly, at 175 km depth-to-slab where the CKD volcanoes are located, crustal fluids would have highly negative $\delta^{11}B$ values. Hence, a fluid contribution from the hydrated slab mantle is indicated. Such serpentinite-derived fluid fluxes at eclogite-facies conditions from the subducted slab mantle have also been postulated in several case studies (Herms et al., 2012; John et al., 2004; Martin et al., 2014), corroborating our interpretation that hydrated slab mantle plays an important role for the water budget in subduction zones.

4. Discussion and Outlook

Both of the examples given in this paper show the immense capacity of combined thermodynamic and trace element models to investigate fluid-rock interaction processes in metamorphic geology. Further, we have shown that boron is a well-suited trace element to trace and quantify fluid-rock interaction at various scales. Our results therefore corroborate the findings of earlier investigations (Bebout and Nakamura 2003; Bebout et al., 2007; Boschi et al., 2008; Bouvier et al., 2008; Brenan et al., 1998; Deyhle et al., 2001; Halama et al., 2014; Ishikawa and Nakamura 1993; Ishikawa and Tera 1997; King et al., 2007; Konrad-Schmolke et al., 2011b; Leeman et al., 1994; Marschall et al., 2007; Nabelek et al., 1990; Pabst et al., 2012; Paquin et al., 2004; Peacock and Hervig 1999; Rose et al., 2000; Sano et al., 2001; Scambelluri et al., 2004; Spivack and Edmond, 1987; Straub and Layne 2002; Tonarini et al., 2001; Wunder et al., 2005) and emphasize the need of more detailed geochemical models that use trace elements and their isotopic composition as a proxy for fluid-rock interaction. At present such complex combined numerical models that focus on the simulation of mass transfer in the solid Earth are at the beginning of unfolding their capacities and more detailed experiments require integration of data and modeling techniques that are still under development.

The two examples presented in this paper diverge in a pivotal aspect: whereas the results of the first example can be directly compared to natural rocks affected by the fluid-rock interaction process, and thus most model parameters can be linked to natural observations, this is not the case in the second, large scale example. Subduction zone models focusing on deep-seated processes, such as the thermal evolution of the subducted slab, the water release and water migration at elevated depth, have generally a large number of unknowns in the

735 boundary conditions of the models, which leads to a high degree of freedom with respect to
736 the interpretation of the model results. Relevant parameters for the mechanical model that is
737 used as basis for the thermodynamic-geochemical model of the Kamchatkan subduction zone
738 comprise rheological parameters, lithological slab structure and the coupling between the slab
739 and the overriding mantle, all of which are specifically discussed in Manea and Manea (2007)
740 and generally in a number of recent papers that concentrate on benchmarking numerical
741 subduction zone models in order to make different approaches comparable (Gerya and Yuen
742 2007; Van Keken et al., 2008; Syracuse et al., 2010). It is beyond the scope of this
743 contribution to test the influence of various parameters on the result of the thermo-mechanical
744 model, but rather to demonstrate the potential of coupled geochemical-thermo-mechanical
745 models to properly interpret geochemical data from arc volcanic rocks – data that is abundant
746 in the literature, but has not yet been implemented into thermo-mechanical subduction zone
747 models (Gerya 2011). As shown in our second example, the implementation of
748 thermomechanical models into thermodynamic and geochemical calculations is crucial for the
749 quantification large-scale elemental fluxes (e.g., Rüpke et al., 2004; Hacker, 2008; Van Keken
750 et al., 2011). The striking coincidence between the water release pattern, the position of
751 volcanic centers in the Kamchatkan arc as well as the B concentration and isotope patterns in
752 the arc volcanic rocks should therefore be seen as stimulation for further research in that field,
753 but also to point out the importance of the subducted slab mantle for the water budget in
754 subduction zones. Furthermore we would like to stress that B and its isotopic composition
755 serve as excellent tracer for these processes. However, the combination of thermomechanical,
756 thermodynamic and trace element models still faces computational obstacles that hinder a
757 complete implementation into a single model. Most thermomechanical models use
758 thermodynamic lookup-tables to constrain mineralogically controlled rheological parameters
759 (e.g., Iwamori, 2007; Arcay et al., 2005) and, in turn, thermodynamic and geochemical
760 models use the thermal pattern from thermomechanical models as basis for their
761 thermodynamic predictions (this study). However, in order to fully quantify mass transfer in
762 three dimensions it will be a major task in geodynamic-geochemical modeling to implement
763 fluid-mediated element transport into thermomechanical models.

764 *4.1. Constraints on fluid migration processes*

765 The mode of fluid transport, e.g. channelized vs. pervasive, as well as the volume and
766 intensity of the fluid-rock interaction process predominantly control the amount and rate of
767 transported solutes (Zack and John 2007). For a correct numerical formulation of

768 thermodynamic-geochemical models the fluid migration mechanism plays a crucial role. In
769 turn, variation of the boundary conditions of such combined models can be used to constrain
770 possible modes of fluid percolation in a particular setting. In nature there are examples of both
771 highly channelized fluid flux in brittle and ductile shear zones (e.g., Bebout and Barton 1993,
772 Austrheim 1987) as well as pervasive fluid flux by interconnected fluid films along grain
773 boundaries (Keller et al., 2006; de Meer et al., 2005, Konrad-Schmolke et al., 2011a, example
774 1 in this work; see also Oliver 1996 for a detailed review) reflecting a broad range of fluid
775 flow mechanisms in natural rocks that might be active at the same time in a single sample
776 (Fusseis and Handy 2008). Several works provide a theoretical background for fluid flux in
777 metamorphic rocks (Connolly and Podlachikov 2007, Fusseis et al., 2009, Kruhl et al., 2013)
778 and numerical thermomechanical models increasingly focus on the prediction and
779 quantification of fluid fluxes in metamorphic rocks, especially in subduction zones (see Gerya
780 2011 and references therein). As metamorphic porosity and thus permeability is transient in
781 most rocks, unequivocal evidence for a certain fluid-migration mode is lacking in most
782 natural samples.

783 Besides experiments that provide insight into porosity development and fluid-induced mineral
784 replacement mechanisms (Putnis and Mezger 2004), natural samples that preserve areas that
785 are unaffected by fluid infiltration together with overprinted parts, such as the samples in our
786 first example, are crucial for the investigation of fluid migration during metamorphism and
787 for the validation of numerical models (Jamtveit et al., 2008; Putnis and Austrheim 2010;
788 Konrad-Schmolke et al., 2011a). Although sensitivity tests allow determination of the critical
789 parameters and give insight into the robustness and validity of numerical model results (e.g.,
790 Spakman and Wortel 2004; Martí et al., 2009; Gray and Pysklywec, 2012), comparison of the
791 modeled processes with their effect on natural rocks is, whenever possible, indispensible. As
792 fluid-rock interaction processes in natural rocks must be investigated from km- to nm-scale
793 and comprise chemical effects that often require high precision combined with high spatial
794 resolution scientific advances in this field are directly coupled with technical innovations
795 (Gianuzzi and Stevie 1999; Albarède et al., 2004; Fusseis et al., 2009; Kylander-Clark et al.,
796 2013). For example, with high-resolution analytical techniques, such as TEM, X-ray
797 tomography using synchrotron radiation or dual beam focused ion beam investigations, syn-
798 metamorphic porosity development can be visualized in natural samples and experiments
799 (e.g., Fusseis et al., 2009, Kruhl et al., 2013) and the sites of fluid rock interaction can be
800 chemically analyzed. However, proper sample selection is of utmost importance in order to
801 trace the effects of fluid rock interaction at various scales. Fig. 14 shows an example of

802 porosity formation in a natural rock from the Franciscan mélange complex at Jenner,
803 California. A metre-sized block of eclogite is partly transformed into blueschist with a clearly
804 visible reaction front running through the block (Fig. 14a). The sharp reaction front separates
805 a moderately affected area where the assemblage clinopyroxene+garnet+rutile is well
806 preserved from a strongly overprinted part with the assemblage
807 glaucophane+plagioclase+titanite (Fig. 14b). One of the strongly zoned clinopyroxene
808 crystals points into the reacted part and the reaction front is running through the lowermost
809 edge of the crystal (Fig. 14c). The electron transparent slice, taken perpendicular to the
810 reaction front (red line in c), shows a µm-sized pore that comprises a dark rim, dark worm-
811 like precipitates and bright Ga precipitate from the FIB sectioning in its interior (Fig. 14d).
812 The dark rim consists of amorphous Si-rich material and is connected with the worm-like
813 material in the interior of the pore (Fig. 14e) that has approximately the same major element
814 composition as the amorphous rim (Fig. 14f and Fig. 15). Precise measurements of major and
815 trace element concentrations and the isotopic compositions in such µm- to nm-scale features
816 displays a challenging task for future analytical developments as such features will reveal the
817 connection between the processes of porosity formation, fluid migration, fluid-rock
818 interaction and metamorphism.

819 Regarding the quantification of element transport – often in the focus of combined
820 thermodynamic-geochemical models – aqueous fluids and hydrous melts have a fundamental
821 importance with respect to the mass transfer in geological systems (e.g., Hermann et al.,
822 2006). In many metamorphic environments, pressures and temperatures exceed the critical
823 point of water resulting in a drastic increase of dissolved material in the transport agent
824 compared to ambient pressures and temperatures (e.g., Manning 1994). Consequently, the
825 thermodynamic and chemical properties of supercritical fluids and hydrous melts control
826 large parts of the mass transfer in the lithosphere. Experiments have shown that the solubility
827 of major and trace elements in supercritical fluids is also strongly dependent on fluid
828 chemistry (e.g., Manning et al., 2008; Wilke et al., 2012). Moreover, solubilities of several
829 elements are enhanced by the addition of ligands (Cl^-, F^-, CO_3^{2-} and SO_4^{2-}) and by complexing
830 with major rock-forming constituents (Antignano and Manning 2008; Tsay et al., 2014). In
831 turn, the fluid chemistry might change along its migration path as a result of the interaction
832 with the wall rock and/or due to changing chemistry of the rock column. Thus, the interaction
833 between fluid chemistry – that may comprise a complete miscibility between hydrous melts
834 and dilute aqueous solutions (Manning, 2004; Hermann et al., 2006) – soluble metal
835 compounds, dissolved trace elements and host rock chemistry controls the fluid-mediated

mass transfer in metamorphic systems. Such reactive fluid flow systems can be quantified with combined thermodynamic-geochemical models. To develop more reliable models additional experimental data as well as knowledge of thermodynamic properties and equations of state of supercritical fluids and the solutes therein are needed (e.g., Hauthal, 2001; Gottschalk et al., 2007; Dolejis and Manning, 2010). Improved analytical instrumentation and experimental setups will allow determination of more precise distribution coefficients, especially those between solid and liquid phases (e.g., Kessel et al., 2005), which are most critical for such trace element models. Determining and quantifying a potential pressure, temperature and host mineral chemistry dependence of the trace element distribution will be essential for forward models that span large pressure and temperature ranges, such as the subduction zone model shown above. Integrating these data in Gibbs energy minimization algorithms, reactive-flow models (e.g. Baumgartner and Ferry 1991) or combined thermodynamic-trace element models (this study) will enable a full quantification of reactive fluid flow and the associated mass transfer in the solid Earth.

4.2. Constraints on thermodynamic and geochemical model parameters

In contrast to most applications in material sciences, simulations of natural processes in geosystems are confronted with complications arising from multiphase-multicomponent chemically open systems that must be simplified in order to be mathematically feasible. In terms of the thermodynamic treatment of the envisaged process much attention must be paid to set appropriate simplified boundary conditions of the model. At first, this concerns the choice of an appropriate chemical system, the selection of thermodynamic datasets and solution models as well as the choice of appropriate thermodynamic variables, such that the boundary conditions of the model reflect the envisaged geological process (e.g., Connolly 2005; Powell et al., 2005). In case of chemically open systems element fractionation processes, such as fluid percolation and fractional crystallization, must be reflected in the models. This circumstance is often disregarded, but has to be considered in order to avoid misinterpretations of thermodynamic equilibrium calculations (Marmo et al., 2002; Konrad-Schmolke et al., 2008a).

The increasing use of phase diagrams in progressively complex chemical systems in the geoscientific literature suggests a rapid development with respect to the understanding of the metamorphic evolution of rock samples. However, as concluded nicely in Powell and Holland (2005), thermodynamic models can be excellently used to solve metamorphic-geodynamic problems as long as the limitations of the available thermodynamic data are known. For

example, significant simplifications must be made with respect to the chemical composition of geosystems in order to make them feasible for mathematic treatment. On the other hand, constraining the chemical system has the disadvantage that the effects of omitted chemical components on the stability of solution phases cannot be predicted. This circumstance is well known for the garnet solid solution, where Mn has a profound influence on garnet stability (e.g., Marmo et al., 2002; Konrad-Schmolke et al., 2005). Furthermore, compositional simplifications of the investigated system often require omission of accessory phases that can play an important role for the trace element budget in metamorphic rocks (e.g., Hermann, 2002). Since thermodynamic data as well trace element distribution coefficients for accessory phases are scarce and contain large uncertainties, incorporation of such phases into thermodynamic and trace element models remains an important task for the future (e.g., Kelsey and Powell, 2010; van Hinsberg et al., 2011).

Many thermodynamic standard state data for chemical endmembers as well as reliable solid solution models for complex phases, such as amphibole and chlorite, are missing and research in this field is work in progress. Modern analytical technology allows determination of precise thermodynamic properties of geologically relevant phases (e.g., Dachs et al., 2009) in calorimetric experiments and improvements have been made to derive more precise activity-composition relationships (e.g., Powell and Holland 2008 and references therein) and equations of state for different geologic environments (e.g., Stixrude and Lithgow-Bertelloni, 2005; Holland and Powell, 2011; Holland et al., 2013). However, none of the published datasets covers the entire range of pressure-, temperature- and compositional variations in geosystems. Regarding the rapidly evolving computational capacities it seems likely that numerical simulations of geomaterials will enable significant developments in thermodynamic applications in geosciences (e.g., van Hinsberg et al., 2005).

Especially in material science and industrial applications (e.g., Dixon and Gutowski 2005) the study of thermodynamic and physical properties of solid and liquid phases involves molecular dynamic and *ab initio* models (e.g., Prausnitz, 1969; Belonoshko and Saxena, 1991; Kalinichev 2001; Cygan, 2001). Both approaches minimize the energy of a given system that is controlled by the electromagnetic forces within and between molecules. Whereas molecular dynamic models require empirical data to model the intra- and intermolecular forces, *ab initio* or quantum mechanical models are directly based on wave functions that describe electron orbitals on the basis of the Schrödinger equations. Consequently, these mathematical approaches require a minimum of empirical data to obtain fundamental thermodynamic

properties of phases, equations of state, physico-chemical properties as well as trace element partition and isotope fractionation coefficients (e.g., Jahn and Wunder 2009; Ottonello et al., 2010; Kowalski et al., 2013; Haigis et al., 2013). Especially the thermodynamic properties of fluids and aqueous species are increasingly simulated utilizing molecular dynamics or *ab initio* models (e.g., Kalinichev 2001 and references therein; Sedlbauer et al., 2000). Due to the immense computational resources needed for these simulations, recent research is focused on simple chemical systems, such as phases in the Earth's mantle or core (e.g., Matsui et al., 2000), but in the near future, numerical atomistic simulations will lead to a better understanding and a prediction of processes in more complex geosystems (e.g., Cruz et al., 2005). In combination with the approach described in van Hinsberg et al., 2005, who derive thermodynamic properties of complex phases by combining the fractional properties of their constituent chemical compounds, *ab inito* models might soon become valuable sources of thermodynamic data for complex phases relevant for geological processes.

Acknowledgements

We thank Vlad Manea for generously providing the thermal model of the Kamchatkan subduction zone and Richard Wirth as well as Anja Schreiber for the TEM analyses and FIB sectioning, respectively. Further, we thank Marco Scambelluri for the invitation to that Review Article and for the editorial handling of the manuscript. We also thank Timm John and an anonymous reviewer for their critical and constructive comments that significantly improved the manuscript. Funding of this work by the Deutsche Forschungsgemeinschaft (grant KO-3750/2-1) is gratefully acknowledged.

926

927

928 **Figure captions**

929 Fig. 1:

930 Two examples of combined thermodynamic-geochemical modeling applied to the
931 petrogenesis of Archean tonalite-trondhjemite-granodiorite (TTG) series rocks (a) and
932 primitive arc magmas (b), respectively. (a) Primitive mantle–normalized trace element
933 patterns of measured Archean TTG rocks from the Isua Supracrustal Belt (gray area) and
934 modeled primitive melt compositions (modified from Nagel et al., 2012). Colored dashed
935 lines represent trace element compositions of the two protoliths considered in the modeling,
936 present-day normal mid-ocean ridge basalt (N-MORB) and Isua tholeiite. Colored solid lines
937 indicate compositions of TTGs modeled for 10% melting at different melting pressures.
938 Characteristic trace element features of natural TTG, including negative Ti and positive Zr-Hf
939 anomalies, are best reproduced by melting of Archean tholeiite at 10-14 kbar, which was
940 considered to represent the source lithology for Archean TTG rocks by Nagel et al. (2012).
941 (b) N-MORB–normalized trace element patterns of arc basalts from the NE Japan arc (red
942 circles) and modeled results from Arc Basalt Simulator (ABS) (modified from Kimura et al.,
943 2009). The thin blue lines mark the minimum and maximum fits calculated by the ABS
944 algorithm. Compositions for the volcanic front were calculated using the Tohoku (NE Japan
945 arc) slab surface trajectory (SST), whereas rear arc compositions were modeled using the
946 Cascadia SST.

947 Fig. 2:

948 (a) Boron isotope data from volcanic arcs in relation to the depth of the subducting slab.
949 Several arcs display decreasing $\delta^{11}B$ values with increasing depth to slab. Notable exceptions
950 are the South Sandwich Islands arc, for which a constant depth is assumed, and the
951 Kamchatka arc, for which $\delta^{11}B$ values are increasing following the typical $\delta^{11}B$ decrease
952 across the volcanic front. (b) Trend of decreasing $\delta^{11}B$ with increasing Nb/B in arc volcanic
953 rocks. The SSI arc deviates from the main trend due to elevated $\delta^{11}B$. Data sources:
954 Kamchatka – Ishikawa et al., 2001; Izu – Ishikawa and Nakamura, 1994; Kuriles – Ishikawa
955 & Tera, 1999; NE Japan – Moriguti et al., 2004; Central Andes – Rosner et al., 2003; South
956 Sandwich Islands –Tonarini et al., 2011; Conical Seamount – Benton et al., 2001; Atlantis
957 Massif – Boschi et al., 2008; MORB – Shaw et al., 2012; AOC – Yamaoka et al., 2012;

Marine sediments – Tonarini et al., 2011; Oceanic basalts – Turner et al., 2007. In (b), data of the other arcs include data shown in (a) and additional data from Smith et al. (1997) and Leeman et al. (2004).

Fig. 3:

Schematic cross section through a subduction zone (modified from Wunder et al., 2005) and sketches of the fluid-rock interaction scenario modeled in this study. Areas of interest are marked by rectangles in the upper sketch. The two lower images show fluid-rock interaction at the slab-wedge interface and recrystallization of phengite and amphibole on the µm to mm scale, as observed in samples from the Sesia Zone. Boron concentrations and $\delta^{11}B$ values typical for natural reservoirs were taken from Wunder et al. (2005) with additional data from Leeman et al. (2004) and Tonarini et al. (2011) for marine sediments and from Spivack and Edmond (1987), Boschi et al. (2008) and Vils et al. (2009) for serpentinized oceanic mantle.

Fig. 4:

a) Back-scattered electron image of partially overprinted phengite from eclogites-facies rocks of the Sesia Zone. Phengite and sodic amphibole grains are compositionally modified along grain boundaries and other fluid pathways. b) Major element microprobe profile along the arrow shown in a). Compositional variations comprise predominantly a Fe-Mg exchange with the other elements being largely unaffected. c) Boron isotopic and concentration data from phengites of the EMS unit in the Sesia Zone (data from Konrad-Schmolke et al., 2011b and Halama et al., 2014). Overprinted areas have consistently lower B contents than the corresponding relict cores, but $\delta^{11}B$ values are similar. Note the coupled decrease in [B] and increase in $\delta^{11}B$ in mylonitic phengite from the shear zone (green arrow).

Fig. 5:

(a) Phase relations and water content in solids in equilibrium assemblage diagrams for sample MK-55 from the Eclogitic Micaschist unit of the Sesia Zone. The diagrams on the left hand side were calculated for peak P-T and water-saturated conditions. The diagrams on the right hand side were calculated with excess H_2O, simulating the fluid influx at 1.35 GPa. (b) X_{Mg} in phengite depending on P and X_{H2O}. The red arrow marks the retrograde path and the blue line represents the water saturation line. Initially, decompression leads to increasingly water-

989 undersaturated conditions in the rock until fluid influx at 1.35 GPa occurs. At these pressures,
990 increasing X_{H2O} causes a significant decrease in X_{Mg}. Mineral abbreviations: qtz = quartz,
991 phng = phengite, pg = paragonite, gln = glaucophane, cpx = clinopyroxene, ep = epidote, lws
992 = lawsonite, pl = plagioclase, chl = chlorite, bt = biotite, cam = clinoamphibole, grt = garnet,
993 mt = magnetite.

994 Fig. 6:

995 Compositional evolution in phengite and modal phase abundances along the retrograde P-T
996 path from 1.45 to 1.1 GPa. Drastic compositional changes are associated with fluid influx at
997 1.35 GPa, causing a decrease in Si_T and X_{Cel} in phengite. Glaucophane, epidote and
998 paragonite abundances increase, whereas omphacite and phengite abundances decrease due to
999 the fluid influx. Mineral abbreviations as in Fig. 1.

1000 Fig. 7:

1001 Fluid-rock interaction model. The evolution of $[B]_{phng}$ and $\delta^{11}B_{phng}$ are shown depending on
1002 the amount of accumulated water (left column) and with decreasing pressure along the
1003 retrograde P-T path (middle column). The range of observed compositional features in relict
1004 phengite cores (green), overprinted phengite rims (red) and mylonitic phengite (blue) are
1005 shown for comparison. In the right column, the relevant parameters are combined to illustrate
1006 how the curves shown in (a) and (b) are linked. The dashed line labeled "fluid influx" marks
1007 the maximum amount of water available before the influx that is consistent with the
1008 composition of the overprinted rims (left column) and the position of the influx on the
1009 retrograde path (middle column).

1010 Fig. 8:

1011 Summary of modeled trends of B release and B isotope fractionation in a slab-derived fluid
1012 during subduction of oceanic crust as modeled by Marschall et al. (2007). Solid lines are B
1013 concentrations, dashed lines are $\delta^{11}B$ values. During subduction, both B concentrations and
1014 $\delta^{11}B$ decrease with increasing pressure. The decrease is particularly strong if there is no
1015 phengite present in the rock.

1016 Fig. 9:

1017 a) A thermal pattern for the Kamchatkan subduction zone derived from the thermomechanical
1018 models of Manea and Manea (2007) was used as basis for the pressure and temperature

relations in the thermodynamic model. The structure of the modeled slab includes all lithologies relevant for the B budget in our models. b) Isotopic fractionation values calculated for the thermal pattern in a) with the data from Wunder et al., 2005.

Fig. 10:

Contoured pseudosection of the modeled slab, subdivided into SSZ wedge mantle, sediments, igneous oceanic crust for dry (a) and hydrated (b) slab mantle. Colored contours show the amount of water in solid phases. Mineral abbreviations as in Fig. 1.

Fig. 11:

Modeled (a) boron concentrations and (b) corresponding $\delta^{11}B_{rock}$ values assuming water-saturated sediments and oceanic crust and a dry slab mantle. The input parameters for wedge mantle (50 µg/g B, $\delta^{11}B$ = +15), sediments (40 µg/g B, $\delta^{11}B$ = +5) and oceanic crust (25 µg/g B, $\delta^{11}B$ = +0.8‰) change during forward modeling due to the fluid-solid B elemental and isotopic fractionation. For the slab mantle, constant values of 0.1 µg/g B and $\delta^{11}B$ = -10‰ are assumed.

Fig. 12:

Modeled dehydration, release of boron and corresponding $\delta^{11}B_{fluid}$ values. (a) SSZ wedge mantle dehydration dominates water release in the forearc. Chlorite breakdown in crust and wedge mantle is the dominant water source at shallow depths down to ~150 km. The marked peak at ~175 km slab surface depth results from serpentine breakdown in the slab mantle. (b) The boron pattern mimics the water release, including high concentrations in the forearc and a prominent peak at ~175 km slab surface depth. (c) High $\delta^{11}B_{fluid}$ values characterize water release into the forearc, followed by a systematic decrease in $\delta^{11}B_{fluid}$ values, reflecting continuous dehydration. The increase in $\delta^{11}B_{fluid}$ at ~175 km slab surface depth is coupled to serpentine dehydration in the slab mantle, and the height of the $\delta^{11}B$ curve depends on water contents in the slab mantle. For a slab mantle hydrated to a depth of 15 km, the best fit is obtained for ~2.5 wt.% H_2O. In all figures, a simplified topographic profile across Kamchatka is shown for comparison. Boron concentration data in (b) are given as B/Nb ratios to eliminate fractionation effects in natural samples. Data from Kamchatka samples are from Ishikawa et al. (2001). Please note that the high frequency variations in the water release are the result of the incremented thermal pattern and does not reflect distinct fluid pulses.

1050 Fig. 13:

1051 Composition of fluids released at the upper boundary of the model into the overlying mantle
1052 wedge. Distinct areas can be defined depending on the dominant water and boron source
1053 lithologies. Fluids derived from the SSZ wedge mantle have the highest B concentrations and
1054 the highest $\delta^{11}B$ values, and all fluids released by mantle deserpentinization have strongly
1055 positive $\delta^{11}B$ values distinct from crustal fluids.

1056 Fig. 14:

1057 Investigation of fluid-rock interaction processes from m- to nm-scale, exemplified by a fluid-
1058 induced blueschist-facies overprint of eclogite from a subduction mélange (Jenner, California,
1059 USA). See text for details.

1060 Fig. 15:

1061 TEM-EDX analyses from areas shown in Fig. 14f. Both the overprinted rim as well as worm-
1062 like structures in the pore interior consist of an amorphous silica-rich material with minor
1063 concentrations of Al, Ca and Fe. Ga and Cu peaks result from the Ga-beam used for FIB
1064 sectioning and the sample holder, respectively.

1065

1066 **References**

1067 Aggarwal, J. K., Palmer, M. R., 1995. Boron isotope analysis. A review. Analyst, 120(5),
1068 1301-1307.

1069 Ague, J.J., 2003. Fluid infiltration and transport of major, minor, and trace elements during
1070 regional metamorphism of carbonate rocks, Wepawaug Schist, Connecticut, USA. American
1071 Journal of Science 303, 753-816.

1072 Ague, J.J., 2011. Extreme channelization of fluid and the problem of element mobility during
1073 Barrovian metamorphism. American Mineralogist 96, 333-352.

1074 Albarède, F., 1995. Introduction to Geochemical Modeling. Cambridge University Press,
1075 Cambridge, 543 pp.

1076 Albarede, F., Telouk, P., Blichert-Toft, J., Boyet, M., Agranier, A., Nelson, B., 2004. Precise
1077 and accurate isotopic measurements using multiple-collector ICPMS. Geochimica et
1078 Cosmochimica Acta, 68(12), 2725-2744.

1079 Altenberger, U., Schmid, R., Oberhänsli, R., 2008. Composition and pre-metamorphic
1080 geodynamic setting of the ultrahigh-pressure metabasic rocks from Dabie Shan, E-China.
1081 International Journal of Earth Sciences 97, 1301-1314.

1082 Angiboust, S., Pettke, T., De Hoog, J.C., Caron, B., Oncken, O., 2014. Channelized Fluid
1083 Flow and Eclogite-facies Metasomatism along the Subduction Shear Zone. Journal of
1084 Petrology, 55(5), 883-916.

1085 Antignano, A., Manning, C.E., 2008. Rutile solubility in H_2O, H_2O–SiO_2, and H_2O–
1086 $NaAlSi_3O_8$ fluids at 0.7–2.0 GPa and 700–1000 C: implications for mobility of nominally
1087 insoluble elements. Chemical Geology, 255, 283-293.

1088 Arcay, D., Tric, E., Doin, M.P., 2005. Numerical simulations of subduction zones: effect of
1089 slab dehydration on the mantle wedge dynamics. Physics of the Earth and Planetary Interiors,
1090 149(1), 133-153.

1091 Asimow, P.D., Ghiorso, M.S., 1998. Algorithmic modifications extending MELTS to
1092 calculate subsolidus phase relations. American Mineralogist 83, 1127-1131.

1093 Austrheim, H., 1987. Eclogitization of lower crustal granulites by fluid migration through
1094 shear zones. Earth and Planetary Science Letters, 81(2), 221-232.

1095 Ayers, J.C., Eggler, D.H., 1995. Partitioning of elements between silicate melt and H_2O-NaCl
1096 fluids at 1.5 and 2.0 GPa pressure: Implications for mantle metasomatism. Geochimica et
1097 Cosmochimica Acta 59, 4237-4246.

1098 Bau, M., 1991. Rare-earth element mobility during hydrothermal and metamorphic fluid-rock
1099 interaction and the significance of the oxidation state of europium. Chemical Geology 93,
1100 219-230.

1101 Baumgartner, L.P., Ferry, J.M., 1991. A model for coupled fluid-flow and mixed-volatile
1102 mineral reactions with applications to regional metamorphism. Contributions to Mineralogy
1103 and Petrology, 106(3), 273-285.

1104 Bebout, G.E., 2007. Metamorphic chemical geodynamics of subduction zones. Earth and
1105 Planetary Science Letters 260, 373-393.

1106 Bebout, G. E., 2013. Metasomatism in subduction zones of subducted oceanic slabs, mantle
1107 wedges, and the slab-mantle interface. In *Metasomatism and the Chemical Transformation of*
1108 *Rock* (pp. 289-349). Springer Berlin Heidelberg.

1109 Bebout, G.E., Barton, M.D., 1993. Metasomatism during subduction: products and possible

paths in the Catalina Schist, California. Chemical Geology, 108(1), 61-92.

Bebout, G.E., Nakamura, E., 2003. Record in metamorphic tourmalines of subduction-zone devolatilization and boron cycling. Geology 31, 407-410.

Bebout, G.E., Ryan, J.G., Leeman, W.P., Bebout, A.E., 1999. Fractionation of trace elements during subduction-zone metamorphism: Impact of convergent margin thermal evolution. Earth and Planetary Science Letters 171, 63-81.

Becker, H., Jochum, K.P., Carlson, R.W., 2000. Trace element fractionation during dehydration of eclogites from high-pressure terranes and the implications for element fluxes in subduction zones. Chemical Geology 163, 65-99.

Beinlich, A., Klemd, R., John, T., Gao, J., 2010. Trace-element mobilization during Ca-metasomatism along a major fluid conduit: Eclogitization of a blueschist as a consequence of fluid-rock interaction. Geochimica et Cosmochimica Acta 74, 1892-1922.

Belonoshko, A., Saxena, S. K., 1991. A molecular dynamics study of the pressure-volume-temperature properties of super-critical fluids: I. H_2O. Geochimica et Cosmochimica Acta 55, 381-387.

Benton, L. D., Ryan, J. G., Tera, F., 2001. Boron isotope systematics of slab fluids as inferred from a serpentine seamount, Mariana forearc. Earth and Planetary Science Letters 187, 273-282.

Berman, R.G., 1988. Internally-consistent thermodynamic data for minerals in the system Na_2O-K_2O-CaO-MgO-FeO-Fe_2O_3-Al_2O_3-SiO_2-TiO_2-H_2O-CO_2. Journal of Petrology 29, 445-522.

Berman, R.G. (1990). Mixing properties of Ca-Mg-Fe-Mn garnets. American Mineralogist 75(3-4): 328-344.

Blundy, J., Wood, B., 2003. Partitioning of trace elements between crystals and melts. Earth and Planetary Science Letters 210, 383-397.

Bohrson, W.A., Spera, F.J., 2001. Energy-constrained open-system magmatic processes II: Application of energy-constrained assimilation-fractional crystallization (EC-AFC) model to magmatic systems. Journal of Petrology 42, 1019-1041.

Bohrson, W.A., Spera, F.J., 2007. Energy-constrained recharge, assimilation, and fractional crystallization (EC-RAχFC): A Visual Basic computer code for calculating trace element and

1140 isotope variations of open-system magmatic systems. Geochemistry Geophysics Geosystems
1141 8(11), Q11003, doi:10.1029/2007GC001781.

1142 Boschi, C., Dini, A., Früh-Green, G.L., Kelley, D.S., 2008. Isotopic and element exchange
1143 during serpentinization and metasomatism at the Atlantis Massif (MAR 30°N): Insights from
1144 B and Sr isotope data. Geochimica et Cosmochimica Acta 72, 1801-1823.

1145 Bouvier, A. S., Metrich, N., Deloule, E., 2008. Slab-derived fluids in the magma sources of
1146 St. Vincent (Lesser Antilles Arc): volatile and light element imprints. Journal of Petrology,
1147 49, 1427-1448.

1148 Breeding, C.M., Ague, J.J., Bröcker, M., 2004. Fluid-metasedimentary rock interactions in
1149 subduction-zone mélange: Implications for the chemical composition of arc magmas.
1150 Geology 32, 1041-1044.

1151 Brenan, J.M., Ryerson, F.J., Shaw, H.F., 1998. The role of aqueous fluids in the slab-to-
1152 mantle transfer of boron, beryllium, and lithium during subduction: Experiments and models.
1153 Geochimica et Cosmochimica Acta 62, 3337-3347.

1154 Brenan, J.M., Shaw, H.F., Ryerson, F.J., Phinney, D.L., 1995. Mineral-aqueous fluid
1155 partitioning of trace elements at 900°C and 2.0 GPa: Constraints on the trace element
1156 chemistry of mantle and deep crustal fluids. Geochimica et Cosmochimica Acta 59, 3331-
1157 3350.

1158 Briscoe, H.V.A., Robinson, P.L., 1925. A redetermination of the atomic weight of boron.
1159 Journal of the Chemical Society 127, 696-720.

1160 Bröcker, M., Baldwin, S., Arkudas, R., 2013. The geological significance of $^{40}Ar/^{39}Ar$ and
1161 Rb-Sr white mica ages from Syros and Sifnos, Greece: a record of continuous
1162 (re)crystallization during exhumation? Journal of Metamorphic Geology 31, 629-646.

1163 Brunsmann, A., Franz, G., Erzinger, J., 2001. REE mobilization during small-scale high-
1164 pressure fluid-rock interaction and zoisite/fluid partitioning of La to Eu. Geochimica et
1165 Cosmochimica Acta 65, 559-570.

1166 Connolly, J.A.D., 2005. Computation of phase equilibria by linear programming: A tool for
1167 geodynamic modeling and its application to subduction zone decarbonation. Earth and
1168 Planetary Science Letters 236, 524-541.

1169 Connolly, J. A. D., Kerrick, D. M., 1987. An algorithm and computer program for calculating
1170 composition phase diagrams. Calphad, 11(1), 1-55.

1171 Connolly, J.A.D., Podladchikov, Y.Y., 2007. Decompaction weakening and channeling
1172 instability in ductile porous media: Implications for asthenospheric melt segregation. Journal
1173 of Geophysical Research: Solid Earth (1978–2012), 112(B10).

1174 Cruz, F. J., Canongia Lopes, J. N., Calado, J. C., & Minas da Piedade, M. E. (2005). A
1175 molecular dynamics study of the thermodynamic properties of calcium apatites. 1. Hexagonal
1176 phases. The Journal of Physical Chemistry B, 109(51), 24473-24479.

1177 Dachs, E., Geiger, C. A., Withers, A. C., Essene, E. J., 2009. A calorimetric investigation of
1178 spessartine: Vibrational and magnetic heat capacity. Geochimica et Cosmochimica Acta
1179 73(11), 3393-3409.

1180 De Capitani, C., Brown, T.H., 1987. The computation of chemical equilibrium in complex
1181 systems containing non-ideal solutions. Geochimica et Cosmochimica Acta 51, 2639-2652.

1182 Cygan, R. T., 2001. Molecular modeling in mineralogy and geochemistry. Reviews in
1183 Mineralogy and Geochemistry, 42(1), 1-35.

1184 de Meer, S., Spiers, C.J., Nakashima, S., 2005. Structure and diffusive properties of fluid-
1185 filled grain boundaries: An in-situ study using infrared (micro) spectroscopy. Earth and
1186 Planetary Science Letters, 232(3), 403-414.

1187 Dempster, T. J., 1992. Zoning and recrystallization of phengitic micas: implications for
1188 metamorphic equilibration. Contributions to Mineralogy and Petrology, 109(4), 526-537.

1189 DePaolo, D.J., 1981. Trace element and isotopic effects of combined wallrock assimilation
1190 and fractional crystallization. Earth and Planetary Science Letters 53, 189-202.

1191 Deyhle, A., Kopf, A., 2005. The use and usefulness of boron isotopes in natural silicate-water
1192 systems. Physics and Chemistry of the Earth 30, 1038-1046.

1193 Deyhle, A., Kopf, A., Eisenhauer, A., 2001. Boron systematics of authigenic carbonates: a
1194 new approach to identify fluid processes in accretionary prisms. Earth and Planetary Science
1195 Letters, 187(1), 191-205.

1196 Di Vincenzo, G., Ghiribelli, B., Giorgetti, G., Palmeri, R., 2001. Evidence of a close link
1197 between petrology and isotope records: constraints from SEM, EMP, TEM and in situ ^{40}Ar-
1198 ^{39}Ar laser analyses on multiple generations of white micas (Lanterman Range, Antarctica).
1199 Earth and Planetary Science Letters 192, 389-405.

1200 Dixon, D. A., Gutowski, M., 2005. Thermodynamic properties of molecular borane amines
1201 and the [BH4-][NH4+] salt for chemical hydrogen storage systems from ab initio electronic
1202 structure theory. The Journal of Physical Chemistry A, 109(23), 5129-5135.

1203 Dolejš, D., Manning, C. E., 2010. Thermodynamic model for mineral solubility in aqueous
1204 fluids: theory, calibration and application to model fluid- flow systems. Geofluids, 10(1- 2),
1205 20-40.

1206 Domanik, K.J., Hervig, R.L., Peacock, S.M., 1993. Beryllium and boron in subduction zone
1207 minerals: An ion microprobe study. Geochimica et Cosmochimica Acta 57, 4997-5010.

1208 Domanik, K.J., Holloway, J.R., 1996. The stability and composition of phengitic muscovite
1209 and associated phases from 5.5 to 11 GPa: Implications for deeply subducted sediments.
1210 Geochimica et Cosmochimica Acta 60, 4133-4150.

1211 Dragovic, B., Samanta, L.M., Baxter, E.F., Selverstone, J., 2012. Using garnet to constrain
1212 the duration and rate of water-releasing metamorphic reactions during subduction: An
1213 example from Sifnos, Greece. Chemical Geology 314-317, 9-22.

1214 Elliott, T., 2003. Tracers of the slab. In: J. Eiler (Editor), Inside the Subduction Factory.
1215 Geophysical Monograph. American Geophysical Union, Washington, DC, pp. 23-45.

1216 Elliott, T., Jeffcoate, A., Bouman, C., 2004. The terrestrial Li isotope cycle: light-weight
1217 constraints on mantle convection. Earth and Planetary Science Letters, 220(3), 231-245.

1218 Essene, E.J., 1989. The current state of thermobarometry in metamorphic rocks. Geol. Soc.
1219 Spec. Publ. 43, 1-44.

1220 Ferry, J.M., Gerdes, M.L., 1998. Chemically reactive fluid flow during metamorphism.
1221 Annual Review of Earth and Planetary Sciences, 26(1), 255-287.

1222 Fusseis, F., Handy, M.R., 2008. Micromechanisms of shear zone propagation at the brittle–
1223 viscous transition. Journal of Structural Geology, 30(10), 1242-1253.

1224 Fusseis, F., Regenauer-Lieb, K., Liu, J., Hough, R.M., De Carlo, F., 2009. Creep cavitation
1225 can establish a dynamic granular fluid pump in ductile shear zones. Nature, 459(7249), 974-
1226 977.

1227 Garth, T., Rietbrock, A., 2014. Order of magnitude increase in subducted H_2O due to
1228 hydrated normal faults within the Wadati-Benioff zone. Geology, doi:10.1130/G34730.1.

1229 Gast, P.W., 1968. Trace element fractionation and the origin of tholeiitic and alkaline magma

1230 types. Geochimica et Cosmochimica Acta 32, 1057-1086.

1231 Ghiorso, M.S., Hirschmann, M.M., Reiners, P.W., Kress, V.C., 2002. The pMELTS: An
1232 revision of MELTS aimed at improving calculation of phase relations and major element
1233 partitioning involved in partial melting of the mantle at pressures up to 3 GPa. Geochemistry
1234 Geophysics Geosystems 3(5), DOI: 10.1029/2001GC000217.

1235 Ghiorso, M.S., Sack, R.O., 1995. Chemical mass transfer in magmatic processes. IV. A
1236 revised and internally consistent thermodynamic model for the interpolation and extrapolation
1237 of liquid-solid equilibria in magmatic systems at elevated temperatures and pressures.
1238 Contributions to Mineralogy and Petrology 119, 197-212.

1239 Giannuzzi, L.A., Stevie, F.A., 1999. A review of focused ion beam milling techniques for
1240 TEM specimen preparation. Micron, 30(3), 197-204.

1241 Glodny, J., Bingen, B., Austrheim, H., Molina, J.F., Rusin, A., 2002. Precise eclogitization
1242 ages deduced from Rb/Sr mineral systematics: The Maksyutov complex, Southern Urals,
1243 Russia. Geochimica et Cosmochimica Acta 66, 1221-1235.

1244 Goldschmidt, V.M., 1937. The principles of distribution of chemical elements in minerals and
1245 rocks. Journal of the Chemical Society 37, 655-673.

1246 Goldschmidt, V.M., 1954. Geochemistry. Clarendon Press, Oxford, 730 pp.

1247 Goncalves, P., Oliot, E., Marquer, D., Connolly, J.A.D., 2012. Role of chemical processes on
1248 shear zone formation: an example from the Grimsel metagranodiorite (Aar massif, Central
1249 Alps). Journal of metamorphic Geology 30, 703-722.

1250 Gorman, P. J., Kerrick, D. M., Connolly, J. A. D., 2006. Modeling open system metamorphic
1251 decarbonation of subducting slabs, Geochem. Geophys. Geosyst., 7, Q04007,
1252 doi:10.1029/2005GC001125.

1253 Gottschalk, M., 1997. Internally consistent thermodynamic data for rock forming minerals.
1254 European Journal of Mineralogy 9, 175-223.

1255 Gottschalk, M., 2007. Equations of state for complex fluids. Reviews in Mineralogy and
1256 Geochemistry, 65(1), 49-97.

1257 Grove, T.L., Till, C.B., Lev, E., Chatterjee, N., Médard, E., 2009. Kinematic variables and
1258 water transport control the formation and location of arc volcanoes. Nature 459, 694-697.

1259 Guidotti, C.V., Sassi, F.P., Blencoe, J.G., Selverstone, J., 1994. The paragonite-muscovite
1260 solvus: I. P-T-X limits derived from the Na-K compositions of natural, quasibinary

paragonite-muscovite pairs. Geochimica et Cosmochimica Acta 58, 2269-2275.

Habler, G., Thöni, M., Miller, C., 2007. Major and trace element chemistry and Sm-Nd age correlation of magmatic pegmatite garnet overprinted by eclogite-facies metamorphism. Chemical Geology 241, 4-22.

Hacker, B. R., 2008. H_2O subduction beyond arcs. Geochemistry, Geophysics, Geosystems, 9(3).

Haigis, V., Salanne, M., Simon, S., Wilke, M., Jahn, S., 2013. Molecular dynamics simulations of Y in silicate melts and implications for trace element partitioning. Chemical Geology, 346, 14-21.

Halama, R., John, T., Herms, P., Hauff, F., Schenk, V., 2011. A stable (Li, O) and radiogenic (Sr, Nd) isotope perspective on metasomatic processes in a subducting slab. Chemical Geology 281, 151-166.

Halama, R., Savov, I.P., Garbe-Schönberg, D., Schenk, V., Toulkeridis, T., 2013. Vesuvianite in high-pressure-metamorphosed oceanic lithosphere (Raspas Complex, Ecuador) and its role for transport of water and trace elements in subduction zones. European Journal of Mineralogy 25, 193-219.

Halama, R., Konrad-Schmolke, M., Sudo, M., Marschall, H.R., Wiedenbeck, M., 2014. Effects of fluid-rock interaction on $^{40}Ar/^{39}Ar$ geochronology in high-pressure rocks (Sesia-Lanzo Zone, Western Alps). Geochimica et Cosmochimica Acta 126, 475-494.

Hattori, K., Guillot, S., 2003. Volcanic fronts form as a consequence of serpentinite dehydration in the forearc mantle wedge. Geology 31, 525-528.

Hauthal, W. H., 2001. Advances with supercritical fluids [review]. Chemosphere, 43(1), 123-135.

Hebert, L.B., Asimow, P., Antoshechkina, P., 2009. Fluid source-based modeling of melt initiation within the subduction zone mantle wedge: Implications for geochemical trends in arc lavas. Chemical Geology 266, 297-310.

Hebert, L. B., Montési, L. G., 2013. Hydration adjacent to a deeply subducting slab: The roles of nominally anhydrous minerals and migrating fluids. Journal of Geophysical Research: Solid Earth, 118(11), 5753-5770.

Helgeson, H.C., Delany, J.M., Nesbitt, H.W., Bird, D.K., 1978. Summary and critique of the

thermodynamic properties of rock-forming minerals. American Journal of Science 278-A, 1-229.

Hermann, J., 2002. Allanite: thorium and light rare earth element carrier in subducted crust. Chemical Geology 192: 289-306.

Hermann, J., Rubatto, D., 2009. Accessory phase control on the trace element signature of sediment melts in subduction zones. Chemical Geology 265, 512-526.

Hermann, J., Spandler, C.J., 2008. Sediment melts at sub-arc depths: an experimental study. Journal of Petrology 49, 717-740.

Hermann, J., Spandler, C., Hack, A., Korsakov, A.V., 2006. Aqueous fluids and hydrous melts in high-pressure and ultra-high pressure rocks: Implications for element transfer in subduction zones. Lithos 92, 399-417.

Herms, P., John, T., Bakker, R.J., Schenk, V. 2012. Evidence for channelized external fluid flow and element transfer in subducting slabs (Raspas Complex, Ecuador). Chemical Geology, 310, 79-96.

Hervig, R.L., Moore, G.M., Williams, L.B., Peacock, S.M., Holloway, J.R., Roggensack, K., 2002. Isotopic and elemental partitioning of boron between hydrous fluid and silicate melt. American Mineralogist 87, 769-774.

Hofmann, A.W., 1997. Mantle geochemistry: the message from oceanic volcanism. Nature, 385, 219-229.

Holland, T. J., Hudson, N. F., Powell, R., Harte, B., 2013. New Thermodynamic Models and Calculated Phase Equilibria in NCFMAS for Basic and Ultrabasic Compositions through the Transition Zone into the Uppermost Lower Mantle. Journal of Petrology, 54(9), 1901-1920.

Holland, T., Blundy, J., 1994. Non-ideal interactions in calcic amphiboles and their bearing on amphibole-plagioclase thermometry. Contributions to Mineralogy and Petrology, 116(4), 433-447.

Holland, T.J.B., Powell, R., 1998. An internally consistent thermodynamic data set for phases of petrologic interest. Journal of metamorphic Geology 16, 309-343.

Holland, T., Powell, R., 2003. Activity–composition relations for phases in petrological calculations: an asymmetric multicomponent formulation. Contributions to Mineralogy and Petrology, 145(4), 492-501.

1321 Holland, T.J.B., Powell, R., 2011. An improved and extended internally consistent
1322 thermodynamic dataset for phases of petrological interest, involving a new equation of state
1323 for solids. Journal of Metamorphic Geology, 29(3), 333-383.

1324 Holloway, J.R., 1977. Fugacity and activity of molecular species in supercritical fluids. In:
1325 Thermodynamics in Geology (ed. Fraser, D) Reidel, Boston, 161-181

1326 Hyndman, R. D., Peacock, S. M., 2003. Serpentinization of the forearc mantle. Earth and
1327 Planetary Science Letters 212(3), 417-432.

1328 Ishikawa, T., Nakamura, E., 1994. Origin of the slab component in arc lavas from across-arc
1329 variation of B and Pb isotopes. Nature 370, 205-208.

1330 Ishikawa, T., Tera, F., 1997. Source, composition and distribution of the fluid in the Kurile
1331 mantle wedge: Constraints from across-arc variations of B/Nb and B isotopes. Earth and
1332 Planetary Science Letters 152, 123-138.

1333 Ishikawa, T., Tera, F., 1999. Two isotopically distinct fluid components involved in the
1334 Mariana arc: Evidence from Nb/B ratios and B, Sr, Nd, and Pb isotope systematics. Geology
1335 27, 83-86.

1336 Ishikawa, T., Tera, F., Nakazawa, T., 2001. Boron isotope and trace element systematics of
1337 the three volcanic zones in the Kamchatka arc. Geochimica et Cosmochimica Acta 65, 4523-
1338 4537.

1339 Iwamori, H., 2007. Transportation of H_2O beneath the Japan arcs and its implications for
1340 global water circulation. Chemical Geology, 239(3), 182-198.

1341 Jacob, D.E., 2006. High sensitivity analysis of trace element-poor geological reference glasses
1342 by Laser ablation-inductively coupled plasma-mass spectrometry (LA-ICP-MS).
1343 Geostandards and Geoanalytical Research 30(3): 221-235.

1344 Jahn, S., Wunder, B., 2009. Lithium speciation in aqueous fluids at high P and T studied by
1345 ab initio molecular dynamics and consequences for Li-isotope fractionation between minerals
1346 and fluids. Geochimica et Cosmochimica Acta, 73(18), 5428-5434.

1347 Jamtveit, B., Malthe-Sørenssen, A., Kostenko, O. 2008. Reaction enhanced permeability
1348 during retrogressive metamorphism. Earth and Planetary Science Letters, 267(3), 620-627.

1349 John, T., Scherer, E.E., Haase, K., Schenk, V., 2004. Trace element fractionation during fluid-
1350 induced eclogitization in a subducting slab: trace element and Lu–Hf–Sm–Nd isotope

systematics. Earth and Planetary Science Letters, 227(3), 441-456.

John, T., Scherer, E., Schenk, V., Herms, P., Halama, R., Garbe-Schönberg, D., 2010. Subducted seamounts in an eclogite-facies ophiolite sequence: The Andean Raspas Complex, SW Ecuador. Contributions to Mineralogy and Petrology 159, 265-284.

John, T., Gussone, N., Podladchikov, Y.Y., Bebout, G.E., Dohmen, R., Halama, R., Klemd, R., Magna, T., Seitz, H.M., 2012. Volcanic arcs fed by rapid pulsed fluid flow through subducting slabs. Nature Geoscience, 5(7), 489-492.

Johnson, J.W., Oelkers, E.H., Helgeson, H.C., 1992. SUPCRT92: A software package for calculating the standard molal thermodynamic properties of minerals, gases, aqueous species and reactions from 1 to 5000 bars and 0 to 1000 °C. Computers & Geosciences 18, 899-947.

Kalinichev, A. G., 2001. Molecular simulations of liquid and supercritical water: thermodynamics, structure, and hydrogen bonding. Reviews in Mineralogy and Geochemistry, 42(1), 83-129.

Kawamoto, T., Yoshikawa, M., Kumagai, Y., Mirabueno, M.H.T., Okuno, M., Kobayashi, T., 2013. Mantle wedge infiltrated with saline fluids from dehydration and decarbonation of subducting slab. Proceedings of the National Academy of Sciences 110, 9663-9668.

Kelemen, P.B., Dick, H.J.B., Quick, J.E., 1992. Formation of harzburgite by pervasive melt/rock reaction in the upper mantle. Nature 358, 635-641.

Keller, L.M., Abart, R., Wirth, R., Schmid, D.W., Kunze, K., 2006. Enhanced mass transfer through short-circuit diffusion: growth of garnet reaction rims at eclogite facies conditions. American Mineralogist, 91(7), 1024-1038.

Kelsey, D.E. and Powell, R., 2010. Progress in linking accessory mineral growth and breakdown to major mineral evolution in metamorphic rocks: a thermodynamic approach in the Na_2O-CaO-K_2O-FeO-MgO-Al_2O_3-SiO_2-H_2O-TiO_2-ZrO_2 system. Journal of Metamorphic Geology 29(1), 151-166.

Kerrick, D. M., Jacobs, G. K., 1981. A modified Redlich-Kwong equation for H_2O, CO_2, and H_2O-CO_2 mixtures at elevated pressures and temperatures. American Journal of Science, 281(6), 735-767.

Kessel, R., Schmidt, M. W., Ulmer, P., and Pettke, T., 2005. Trace element signature of subduction-zone fluids, melts and supercritical liquids at 120–180 km depth. Nature, 437(7059), 724-727.

1382 Kimura, J. I., Hacker, B. R., van Keken, P. E., Kawabata, H., Yoshida, T., Stern, R. J., 2009.
1383 Arc Basalt Simulator version 2, a simulation for slab dehydration and fluid- fluxed mantle
1384 melting for arc basalts: Modeling scheme and application. Geochemistry, Geophysics,
1385 Geosystems, 10(9).

1386 Kimura, J. I., Kent, A. J., Rowe, M. C., Katakuse, M., Nakano, F., Hacker, B. R., Stern, R. J.,
1387 2010. Origin of cross- chain geochemical variation in Quaternary lavas from the northern Izu
1388 arc: Using a quantitative mass balance approach to identify mantle sources and mantle wedge
1389 processes. Geochemistry, Geophysics, Geosystems, 11(10).

1390 Kimura, J.I., Gill, J.B., Kunikiyo, T., Osaka, I., Shimoshioiri, Y., Katakuse, M., Kakubuchi,
1391 S., Nagao, T., Furuyama, K., Kamei, A., Kawabata, H., Nakajima, J., van Keken, P.E., Stern,
1392 R.J., 2014. Diverse magmatic effects of subducting a hot slab in SW Japan: results from
1393 forward modeling. Geochemistry Geophysics Geosystems, doi: 10.1002/2013GC005132.

1394 King, R. L., Bebout, G. E., Grove, M., Moriguti, T., and Nakamura, E., 2007. Boron and lead
1395 isotope signatures of subduction-zone mélange formation: hybridization and fractionation
1396 along the slab–mantle interface beneath volcanic arcs. Chemical Geology 239(3), 305-322.

1397 Kohn, M.J., 2003. Geochemical zoning in metamorphic minerals. In: Rudnick, R.L. (Ed), *The*
1398 *Crust*, Treatise on Geochemistry, 3, Elsevier, pp. 229-261.

1399 Konrad-Schmolke, M., Handy, M. R., Babist, J., O'Brien, P. J., 2005. Thermodynamic
1400 modelling of diffusion-controlled garnet growth. Contributions to Mineralogy and Petrology,
1401 149(2), 181-195.

1402 Konrad-Schmolke, M., O'Brien, P. J., Heidelbach, F., 2007. Compositional re-equilibration of
1403 garnet: The importance of sub-grain boundaries. European Journal of Mineralogy 19(4), 431-
1404 438.

1405 Konrad-Schmolke, M., O'Brien, P.J., De Capitani, C., Carswell, D.A., 2008a. Garnet growth
1406 at high- and ultra-high pressure conditions and the effect of element fractionation on mineral
1407 modes and composition. Lithos 103, 309-332.

1408 Konrad-Schmolke, M., O'Brien, P.J., Zack, T., 2011a. Fluid migration above a subducted slab
1409 - constraints on amount, pathways and major element mobility from partially overprinted
1410 eclogite-facies rocks (Sesia Zone, Western Alps). Journal of Petrology 52, 457-486.

1411 Konrad-Schmolke, M., Zack, T., O'Brien, P.J., Barth, M., 2011b. Fluid migration above a

1412 subducted slab - thermodynamic and trace element modelling of fluid-rock interaction in
1413 partially overprinted eclogite-facies rocks (Sesia Zone, Western Alps). Earth and Planetary
1414 Science Letters 311, 287-298.

1415 Konrad-Schmolke, M., Zack, T., O'Brien, P.J., Jacob, D., 2008b. Combined thermodynamic
1416 and rare earth element modelling of garnet growth during subduction: Examples from
1417 ultrahigh-pressure eclogite of the Western Gneiss Region, Norway. Earth and Planetary
1418 Science Letters 272, 488-498.

1419 Korzhinskii, D.S., 1965. The theory of systems with perfectly mobile components and
1420 processes of mineral formation. Am. J. Sci. 263: 193-205.

1421 Koukarri, P., Pajarre, R. 2011. A Gibbs energy minimization method for constrained and
1422 partial equilibria. Pure and Applied Chemistry (83), 6: 1243-1254.

1423 Kowalski, P. M., Wunder, B., Jahn, S., 2013. Ab initio prediction of equilibrium boron
1424 isotope fractionation between minerals and aqueous fluids at high P and T. Geochimica et
1425 Cosmochimica Acta, 101, 285-301.

1426 Kruhl, J. H., Wirth, R., Morales, L. F. (2013): Quartz grain boundaries as fluid pathways in
1427 metamorphic rocks. - Journal of Geophysical Research, 118, 5, p. 1957-1967.

1428 Kulik, D.A., Berner, U., Curti, E., 2004. Modelling chemical equilibrium partitioning with the
1429 GEMS-PSI code, Paul Scherrer Institute, Villigen, Switzerland.

1430 Kulik, D.A., Wagner, T., Dmytrieva, S.V., Kosakowski, G., Hingerl, F.F., Chudnenko, K.V.,
1431 Berner, U., 2013. GEM-Selektor geochemical modeling package: revised algorithm and
1432 GEMS3K numerical kernel for coupled simulation codes. Computational Geosciences 17, 1-
1433 24.

1434 Kylander-Clark, A.R., Hacker, B.R., Cottle, J.M., 2013. Laser-ablation split-stream ICP
1435 petrochronology. Chemical Geology, 345, 99-112.

1436 Leeman, W. P., Carr, M. J., Morris, J. D., 1994. Boron geochemistry of the Central American
1437 volcanic arc: Constraints on the genesis of subduction-related magmas. Geochimica et
1438 Cosmochimica Acta, 58(1), 149-168.

1439 Leeman, W.P., Tonarini, S., Chan, L.-H., Borg, L.E., 2004. Boron and lithium isotopic
1440 variations in a hot subduction zone - the southern Washington Cascades. Chemical Geology
1441 212, 101-124.

1442 Manea, V.C., Manea, M., 2007. Thermal models beneath Kamchatka and the Pacific plate

1443 rejuvenation from a mantle plume impact. In: J. Eichelberger, P. Izbekov, N. Ruppert, E.
1444 Gordeev and J. Lees (Editors), Volcanism and Tectonics of the Kamchatka peninsula and
1445 adjacent arcs, Geophysical Monograph Series. Geophysical Monograph Series, pp. 77-90.

1446 Manning, C. E., 2004. The chemistry of subduction-zone fluids. Earth and Planetary Science
1447 Letters 223, (1-2): 1-16.

1448 Manning, C.E., Wilke, M., Schmidt, C., Cauzid, J., 2008. Rutile solubility in albite-H_2O and
1449 $Na_2Si_3O_7$-H_2O at high temperatures and pressures by in-situ synchrotron radiation micro-
1450 XRF. Earth and Planetary Science Letters, 272(3-4), 730-737.

1451 Margules, M., 1895. Über die Zusammensetzung der gesättigten Dämpfe von Mischungen.
1452 Sitzungsberichte der Kaiserliche Akademie der Wissenschaften Wien Mathematisch-
1453 Naturwissenschaftliche Klasse II 104, 1243–1278.

1454 Marmo, B.A., Clarke, G.L., Powell, R., 2002. Fractionation of bulk rock composition due to
1455 porphyroblast growth: effects on eclogite facies mineral equilibria, Pam Peninsula, New
1456 Caledonia. Journal of Metamorphic Geology 20(1): 151-165.

1457 Marschall, H.R., Altherr, R., Gméling, K., Kasztovszky, Z., 2009. Lithium, boron and
1458 chlorine as tracers for metasomatism in high-pressure metamorphic rocks: a case study from
1459 Syros (Greece). Mineralogy and Petrology.

1460 Marschall, H.R., Altherr, R., Ludwig, T., Kalt, A., Gméling, K., Kasztovszky, Z., 2006.
1461 Partitioning and budget of Li, Be and B in high-pressure metamorphic rocks. Geochimica et
1462 Cosmochimica Acta 70, 4750-4769.

1463 Marschall, H.R., Altherr, R., Rüpke, L., 2007. Squeezing out the slab - modelling the release
1464 of Li, Be and B during progressive high-pressure metamorphism. Chemical Geology 239,
1465 323-335.

1466 Martin, L.A., Rubatto, D., Crépisson, C., Hermann, J., Putlitz, B., Vitale-Brovarone, A., 2014.
1467 Garnet oxygen analysis by SHRIMP-SI: Matrix corrections and application to high-pressure
1468 metasomatic rocks from Alpine Corsica. Chemical Geology, 374, 25-36.

1469 Massonne, H.-J., Schreyer, W., 1987. Phengite geobarometry based on the limiting
1470 assemblage with K-feldspar, phlogopite, and quartz. Contributions to Mineralogy and
1471 Petrology 96, 212-224.

1472 Matsui, M., Parker, S. C., & Leslie, M. (2000). The MD simulation of the equation of state of
1473 MgO: Application as a pressure calibration standard at high temperature and high pressure.
1474 American Mineralogist, 85(2), 312-316.

1475 McKenzie, D., O'Nions, R.K., 1991. Partial melt distributions from inversion of Rare Earth
1476 Element concentrations. Journal of Petrology 32, 1021-1091.

1477 Moriguti, T., Nakamura, E., 1998. Across-arc variation of Li isotopes in lavas and
1478 implications for crust/mantle recycling at subduction zones. Earth and Planetary Science
1479 Letters 163, 167-174.

1480 Moriguti, T., Shibata, T., Nakamura, E., 2004. Lithium, boron and lead isotope and trace
1481 element systematics of Quaternary basaltic volcanic rocks in northeastern Japan:
1482 mineralogical controls on slab-derived fluid composition. Chemical Geology 212, 81-100.

1483 Morris, J.D., Leeman, W.P., Tera, F., 1990. The subducted component in island arc lavas:
1484 constraints from Be isotopes and B-Be systematics. Nature 344, 31-36.

1485 Nabelek, P.I., 1987. General equations for modeling fluid/rock interaction using trace
1486 elements and isotopes. Geochimica et Cosmochimica Acta, 51(6), 1765-1769.

1487 Nabelek, P. I., Denison, J. R., Glascock, M. D., 1990. Behavior of boron during contact
1488 metamorphism of calc-silicate rocks at Notch Peak, Utah. American Mineralogist, 75(7-8),
1489 874-880.

1490 Nagel, T.J., Hoffmann, J.E., Münker, C., 2012. Generation of Eoarchean tonalite-
1491 trondhjemite-granodiorite series from thickened mafic arc crust. Geology 40, 375-378.

1492 O'Hara, M.J., 1977. Geochemical evolution during fractional crystallization of a periodically
1493 refilled magma chamber. Nature 266, 503-507.

1494 Oelkers, E.H., Bénézeth, P., Pokrovski, G.S., 2009. Thermodynamic databases for water-rock
1495 interaction. Reviews in Mineralogy and Geochemistry 70, 1-56.

1496 Oliver, N.H.S., 1996. Review and classification of structural controls on fluid flow during
1497 regional metamorphism. Journal of Metamorphic Geology, 14(4), 477-492.

1498 Ottonello, G., Civalleri, B., Ganguly, J., Perger, W.F., Belmonte, D., Zuccolini, M.V., 2010.
1499 Thermo-chemical and thermo-physical properties of the high-pressure phase anhydrous B
1500 ($Mg_{14}Si_5O_{24}$): An ab-initio all-electron investigation. American Mineralogist, 95(4), 563-573.

1501 Pabst, S., Zack, T., Savov, I.P., Ludwig, T., Rost, D., Vicenzi, E.P., 2011. Evidence for boron
1502 incorporation into the serpentine crystal structure. American Mineralogist 96, 1112-1119.

Pabst, S., Zack, T., Savov, I.P., Ludwig, T., Rost, D., Tonarini, S., Vicenzi, E.P., 2012. The fate of subducted oceanic slabs in the shallow mantle: Insights from boron isotopes and light element composition of metasomatized blueschists from the Mariana forearc. Lithos 132-133, 162-179.

Padrón-Navarta, J. A., Sánchez-Vizcaíno, V. L., Hermann, J., Connolly, J. A., Garrido, C. J., Gómez-Pugnaire, M. T., & Marchesi, C. (2013). Tschermak's substitution in antigorite and consequences for phase relations and water liberation in high-grade serpentinites. Lithos, 178, 186-196.

Paquin, J., Altherr, R., and Ludwig, T., 2004. Li–Be–B systematics in the ultrahigh-pressure garnet peridotite from Alpe Arami (Central Swiss Alps): implications for slab-to-mantle wedge transfer. Earth and Planetary Science Letters, 218(3), 507-519.

Parkhurst, D.L., Appelo, C.A.J., 1999. User's guide to PHREEQC (version 2) - a computer program for speciation, batch-reaction, one-dimensional transport, and inverse geochemical calculations.

Peacock, S.M., Hervig, R.L., 1999. Boron isotopic composition of subduction-zone metamorphic rocks. Chemical Geology 160, 281-290.

Pearce, J.A., Peate, D.W., 1995. Tectonic implications of the composition of volcanic arc magmas. Annu. Rev. Earth Planet. Sci. 23, 251-285.

Pearce, J.A., 2008. Geochemical fingerprinting of oceanic basalts with applications to ophiolite classification and the search for Archean oceanic crust. Lithos, 100(1), 14-48.

Pearce, M.A., Wheeler, J., 2010. Modelling grain-recycling zoning during metamorphism. Journal of metamorphic Geology 28, 423-437.

Plank, T., Langmuir, C.H., 1993. Tracing trace elements from sediment input to volcanic output at subduction zones. Nature 362, 739-743.

Plank, T., Langmuir, C. H. 1998. The chemical composition of subducting sediment and its consequences for the crust and mantle. Chem. Geol. 145, 325-394.

Pollington, A.D., Baxter, E.F., 2010. High resolution Sm-Nd garnet geochronology reveals the uneven pace of tectonometamorphic processes. Earth and Planetary Science Letters 293, 63-71.

Powell, R., Holland, T.J.B., 1988. An internally consistent data set with uncertainties and correlations: 3. Applications to geobarometry, worked examples and a computer program.

Journal of Metamorphic Geology 6, 173-204.

Powell, R., Holland, T. J. B., 2008. On thermobarometry. Journal of Metamorphic Geology, 26(2), 155-179.

Powell, R., Guiraud, M., White, R.W., 2005. Truth and beauty in metamorphic phase-equilibria: conjugate variables and phase diagrams. The Canadian Mineralogist, 43(1), 21-33.

Prausnitz, J.M., 1969. Molecular Thermodynamics of Fluid-Phase Equilibria, 523 pp. Prentice-Hall.

Putnis, C.V., Mezger, K., 2004. A mechanism of mineral replacement: isotope tracing in the model system KCl-KBr-H_2O. Geochimica et Cosmochimica Acta, 68(13), 2839-2848.

Putnis, A., Austrheim, H., 2010. Fluid- induced processes: metasomatism and metamorphism. Geofluids, 10(1- 2), 254-269.

Ranero, C.R., Phipps Morgan, J., McIntosh, K., Reichert, C., 2003. Bending-related faulting and mantle serpentinization at the Middle American trench. Nature 425, 367-373.

Ranero, C.R., Sallarès, V., 2004. Geophysical evidence for hydration of the crust and mantle of the Nazca plate during bending at the north Chile trench. Geology 32, 549-552.

Redlich, O. and Kwong, J.N.S., 1949. An equation of state. Fugacities of gaseous solutions. Chem. Rev. 44: 233-244.

Robie, R.A. and Hemingway, B.S. 1995. Thermodynamic Properties of Minerals and Related Substances at 298.15 K and 1 Bar (10^5 Pascals) Pressure and at Higher Temperature, U. S. Geological Survey, Washington, DC, 461 pp.

Rose, E. F., Chaussidon, M., France-Lanord, C., 2000. Fractionation of boron isotopes during erosion processes: the example of Himalayan rivers. Geochimica et Cosmochimica Acta 64(3), 397-408.

Rosner, M., Erzinger, J., Franz, G., Trumbull, R.B., 2003. Slab-derived boron isotope signatures in arc volcanic rocks from the Central Andes and evidence for boron isotope fractionation during progressive slab dehydration. Geochemistry Geophysics Geosystems 4(8), 9005, doi:10.1029/2002GC000438.

Rosner, M., Wiedenbeck, M., and Ludwig, T., 2008. Composition- induced variations in SIMS instrumental mass fractionation during boron isotope ratio measurements of silicate glasses. Geostandards and Geoanalytical Research 32(1), 27-38.

1564 Rüpke, L. H., Morgan, J. P., Hort, M., and Connolly, J. A., 2004. Serpentine and the
1565 subduction zone water cycle. Earth and Planetary Science Letters 223(1), 17-34.

1566 Rüpke, L., Phipps Morgan, J., and Eaby Dixon, J., 2006. Implications of subduction
1567 rehydration for Earth's deep water cycle. Geophysical Monograph Series, 168, 263-276.

1568 Ryan, J., Morris, J., Bebout, G.E., Leeman, W.P., 1996. Describing chemical fluxes in
1569 subduction zones: insights from "depth-profiling" studies of arc and forearc rocks. In: G.E.
1570 Bebout, D.W. Scholl, S.H. Kirby and J.P. Platt (Editors), Subduction top to bottom. American
1571 Geophysical Union Monograph, pp. 263-268.

1572 Ryan, J., Morris, J., Tera, F., Leeman, W.P., Tsvetkov, A., 1995. Cross-arc geochemical
1573 variations in the Kurile arc as a function of slab depth. Science 270, 625-627.

1574 Ryan, J.G., Langmuir, C.H., 1993. The systematics of boron abundances in young volcanic
1575 rocks. Geochimica et Cosmochimica Acta 57, 1489-1498.

1576 Ryan, J.G. and Chauvel, C., 2013. The Subduction Zone Conveyor and the Impact of
1577 Recycled Materials on the Evolution of the Mantle. Chapter 2.11 The Mantle and Core
1578 (Carlson, R. Ed.), Treatise on Geochemistry, Second Edition (in press)

1579 Sanchez-Valle, C., Reynard, B., Daniel, I., Lecuyer, C., Martinez, I., Chervin, J.-C., 2005.
1580 Boron isotopic fractionation between minerals and fluids: New insights from in situ high
1581 pressure-high temperature vibrational spectroscopic data. Geochimica et Cosmochimica Acta
1582 69, 4301-4313.

1583 Sano, T., Hasenaka, T., Shimaoka, A., Yonezawa, C., and Fukuoka, T., 2001. Boron contents
1584 of Japan Trench sediments and Iwate basaltic lavas, Northeast Japan arc: estimation of
1585 sediment-derived fluid contribution in mantle wedge. Earth and Planetary Science Letters,
1586 186(2), 187-198.

1587 Savov, I.P., Ryan, J.G., D'Antonio, M., Fryer, P., 2007. Shallow slab fluid release across and
1588 along the Mariana arc-basin system: Insights from geochemistry of serpentinized peridotites
1589 from the Mariana fore arc. Journal of Geophysical Research 112, B09205,
1590 doi:10.1029/2006JB004749.

1591 Savov, I.P., Ryan, J.G., D'Antonio, M., Kelley, K., Mattie, P., 2005. Geochemistry of
1592 serpentinized peridotites from the Mariana Forearc Conical Seamount, ODP Leg 125:
1593 Implications for the elemental recycling at subduction zones. Geochemistry Geophysics
1594 Geosystems 6, Q04J15, doi:10.1029/2004GC000777.

1595 Scambelluri, M., Bottazzi, P., Trommsdorff, V., Vannucci, R., Hermann, J., Gómez-Pugnaire,
1596 M.T., López-Sánchez Vizcaíno, V., 2001. Incompatible element-rich fluids released by
1597 antigorite breakdown in deeply subducted mantle. Earth and Planetary Science Letters 192,
1598 457-470.

1599 Scambelluri, M., Müntener, O., Ottolini, L., Pettke, T., Vannucci, R., 2004. The fate of B, Cl
1600 and Li in the subducted oceanic mantle and in antigorite breakdown fluids. Earth and
1601 Planetary Science Letters 222, 217-234.

1602 Scambelluri, M., Tonarini, S., 2012. Boron isotope evidence for shallow fluid transfer across
1603 subduction zones by serpentinized mantle. Geology 40, 907-910.

1604 Schmidt, M.W., Poli, S. 1998. Experimentally based water budgets for dehydrating slabs and
1605 consequences for arc magma generation. Earth and Planetary Science Letters, 163(1), 361-
1606 379.

1607 Sedlbauer, J., O'Connell, J.P., Wood, R.H., 2000. A new equation of state for correlation and
1608 prediction of standard molal thermodynamic properties of aqueous species at high
1609 temperatures and pressures. Chemical Geology, 163(1), 43-63.

1610 Selverstone, J., Morteani, G., Staude, J.-M., 1991. Fluid channelling during ductile shearing:
1611 transformation of granodiorite into aluminous schist in the Tauern Window, Eastern Alps.
1612 Journal of metamorphic Geology 9, 419-431.

1613 Sharp, Z., 2007. Principles of Stable Isotope Geochemistry. Pearson Prentice Hall, Upper
1614 Saddle River, New Jersey, 344 pp.

1615 Shaw, D.M., 1970. Trace element fractionation during anatexis. Geochimica et
1616 Cosmochimica Acta 34, 237-243.

1617 Shaw, A.M., Hauri, E.H., Behn, M.D., Hilton, D.R., Macpherson, C.G., Sinton, J.M., 2012.
1618 Long-term preservation of slab signatures in the mantle inferred from hydrogen isotopes.
1619 Nature Geoscience 5, 224-228.

1620 Simon, L., Lécuyer, C., Maréchal, C., and Coltice, N., 2006. Modelling the geochemical cycle
1621 of boron: Implications for the long-term $\delta^{11}B$ evolution of seawater and oceanic crust.
1622 Chemical Geology 225(1), 61-76.

1623 Skora, S., Baumgartner, L. P., Mahlen, N. J., Johnson, C. M., Pilet, S., and Hellebrand, E.,
1624 2006. Diffusion-limited REE uptake by eclogite garnets and its consequences for Lu–Hf and
1625 Sm–Nd geochronology. Contributions to Mineralogy and Petrology, 152(6), 703-720.

1626 Smith, H.J., Leeman, W.P., Davidson, J., Spivack, A.J., 1997. The B isotopic composition of
1627 arc lavas from Martinique, Lesser Antilles. Earth and Planetary Science Letters 146, 303-314.

1628 Sorensen, S.S., Grossman, J.N., 1989. Enrichment of trace elements in garnet amphibolites
1629 from a paleo-subduction zone: Catalina Schist, southern California. Geochimica et
1630 Cosmochimica Acta 53, 3155-3177.

1631 Spandler, C., Pirard, C., 2013. Element recycling from subducting slabs to arc crust: A
1632 review. Lithos 170-171, 208-223.

1633 Spear, F.S., 1988. Metamorphic fractional crystallization and internal metasomatism by
1634 diffusional homogenization of zoned garnets. Contributions to Mineralogy and Petrology 99,
1635 507-517.

1636 Spear, F.S., Menard, T., 1989. Program GIBBS: A generalized Gibbs method algorithm.
1637 American Mineralogist 74, 942-943.

1638 Spear, F.S., Selverstone, J., 1983. Quantitative P-T paths from zoned minerals: Theory and
1639 tectonic applications. Contributions to Mineralogy and Petrology 83, 348-357.

1640 Spivack, A.J., Edmond, J.M., 1987. Boron isotope exchange between seawater and the
1641 oceanic crust. Geochimica et Cosmochimica Acta 51, 1033-1043.

1642 Stixrude, L., and Lithgow- Bertelloni, C., 2005. Thermodynamics of mantle minerals–I.
1643 Physical properties. Geophysical Journal International 162(2), 610-632.

1644 Straub, S.M., Layne, G.D., 2003. The systematics of chlorine, fluorine, and water in Izu arc
1645 front volcanic rocks: Implications for volatile recycling in subduction zones. Geochimica et
1646 Cosmochimica Acta 67, 4179-4203.

1647 Tatsumi, Y., Hamilton, D.L., Nesbitt, R.W., 1986. Chemical characteristics of fluid phase
1648 released from a subducted lithosphere and origin of arc magmas: evidence from high-pressure
1649 experiments and natural rocks. Journal of Volcanology and Geothermal Research 29, 293-
1650 309.

1651 Taura, H., Yurimoto, H., Kurita, K., Sueno, S., 1998. Pressure dependence on partition
1652 coefficients for trace elements between olivine and the coexisting melts. Contributions to
1653 Mineralogy and Petrology 25, 469-484.

1654 Taylor, J.H.P., Epstein, S., 1962. Relationship between O^{18}/O^{16} ratios in coexisting minerals
1655 of igneous and metamorphic rocks, Part 2: Application to petrologic problems. . Geological
1656 Society of America Bulletin 73, 675-694.

1657 Thompson, A.B., England, P.C., 1984. Pressure—Temperature—Time Paths of Regional
1658 Metamorphism II. Their Inference and Interpretation using Mineral Assemblages in
1659 Metamorphic Rocks. Journal of Petrology, 25(4), 929-955.

1660 Till, C.B., Grove, T.L., Withers, A., 2012. The beginnings of hydrous mantle wedge melting.
1661 Contributions to Mineralogy and Petrology 163, 669-688.

1662 Tonarini, S., Armienti, P., D'Orazio, M., Innocenti, F., 2001. Subduction-like fluids in the
1663 genesis of Mt. Etna magmas: evidence from boron isotopes and fluid mobile elements. Earth
1664 and Planetary Science Letters 192, 471-483.

1665 Tonarini, S., Agostini, S., Doglioni, C., Innocenti, F., Manetti, P., 2007. Evidence for
1666 serpentinite fluid in convergent margin systems: The example of El Salvador (Central
1667 America) arc lavas. Geochemistry Geophysics Geosystems 8, Q09014,
1668 doi:10.1029/2006GC001508.

1669 Tonarini, S., Leeman, W.P., Leat, P.T., 2011. Subduction erosion of forearc mantle wedge
1670 implicated in the genesis of the South Sandwich Island (SSI) arc: Evidence from boron
1671 isotope systematics. Earth and Planetary Science Letters 301, 275-284.

1672 Trumbull, R.B., Krienitz, M.-S., Gottesmann, B., Wiedenbeck, M., 2008. Chemical and
1673 boron-isotope variations in tourmalines from an S-type granite and its source rocks: the
1674 Erongo granite and tourmalinites in the Damara Belt, Namibia. Contributions to Mineralogy
1675 and Petrology 155, 1-18.

1676 Trumbull, R.B., Krienitz, M.-S., Grundmann, G., Wiedenbeck, M., 2009. Tourmaline
1677 geochemistry and $d^{11}B$ variations as a guide to fluid-rock interaction in the Habachtal emerald
1678 deposit, Tauern Window, Austria. Contributions to Mineralogy and Petrology 157, 411-427.

1679 Tsay, A., Zajacz, Z., Sanchez-Valle, C., 2014. Efficient mobilization and fractionation of rare-
1680 earth elements by aqueous fluids upon slab dehydration. Earth and Planetary Science Letters,
1681 398, 101-112.

1682 Turner, S., Tonarini, S., Bindeman, I., Leeman, W.P., Schaefer, B.F., 2007. Boron and
1683 oxygen isotope evidence for recycling of subducted components over the past 2.5 Gyr. Nature
1684 447, 702-705.

1685 Ulmer, P., Trommsdorff, V., 1995. Serpentine stability to mantle depths and subduction-
1686 related magmatism. Science 268, 858-861.

1687 Valle, N., Drillet, J., Pic, A., Migeon, H. N., 2011. Nano- SIMS investigation of boron

distribution in steels. Surface and Interface Analysis 43(1- 2), 573-575.

van der Straaten, F., Halama, R., John, T., Schenk, V., Hauff, F., Andersen, N., 2012. Tracing the effects of high-pressure metasomatic fluids and seawater alteration in blueschist-facies overprinted eclogites: Implications for subduction channel processes. Chemical Geology 292-293, 69-87.

Van Hinsberg, V. J., Vriend, S. P., Schumacher, J. C. (2005). A new method to calculate end- member thermodynamic properties of minerals from their constituent polyhedra I: enthalpy, entropy and molar volume. Journal of Metamorphic Geology 23(3), 165-179.

Van Hinsberg, V. J., Henry, D. J., Dutrow, B. L., 2011. Tourmaline as a petrologic forensic mineral: A unique recorder of its geologic past. Elements 7(5), 327-332.

van Keken, P. E., Hacker, B. R., Syracuse, E. M., Abers, G. A., 2011. Subduction factory: 4. Depth- dependent flux of H_2O from subducting slabs worldwide. Journal of Geophysical Research 116, B01401.

Van Laar, J.J., 1910. Ueber Dampfspannung von binären Gemischen. Zeitschrift für Physikalische Chemie 72, 723-751.

Velde, B., 1965. Phengite micas: Synthesis, stability, and natural occurrence. American Journal of Science 263, 886-913.

Vils, F., Tonarini, S., Kalt, A., Seitz, H.-M., 2009. Boron, lithium and strontium isotopes as tracers of seawater-serpentinite interaction at Mid-Atlantic ridge, ODP leg 209. Earth and Planetary Science Letters 286, 414-425.

Warren, C.J., Kelley, S.P., Sherlock, S.C., McDonald, C.S., 2012. Metamorphic rocks seek meaningful cooling rate: Interpreting $^{40}Ar/^{39}Ar$ ages in an exhumed ultra-high pressure terrane. Lithos 155, 30-48.

Warren, C.J., Sherlock, S.C., Kelley, S.P., 2011. Interpreting high-pressure phengite $^{40}Ar/^{39}Ar$ laserprobe ages: an example from Saih Hatat, NE Oman. Contributions to Mineralogy and Petrology 161, 991-1009.

Weaver, B.L., 1991. Trace element evidence for the origin of ocean-island basalts. Geology 19, 123-126.

White, W.M., 2013. Geochemistry. Wiley-Blackwell, Chichester, 660 pp.

Wilke, M., Schmidt, C., Dubrail, J., Appel, K., Borchert, M., Kvashnina, K., Manning, C.E.,

2012. Zircon solubility and zirconium complexation in H_2O+ Na_2O+ SiO_2±Al_2O_3 fluids at high pressure and temperature. Earth and Planetary Science Letters, 349, 15.

Workman, R. K., Hart, S. R. 2005. Major and trace element composition of the depleted MORB mantle (DMM). Earth Planet. Sci. Lett. 231, 53-72.

Wunder, B., Meixner, A., Romer, R.L., Wirth, R., Heinrich, W., 2005. The geochemical cycle of boron: Constraints from boron isotope partitioning experiments between mica and fluid. Lithos 84, 205-216.

Yamaoka, K. et al., 2012. Boron and oxygen isotope systematics for a complete section of oceanic crustal rocks in the Oman ophiolite. Geochimica et Cosmochimica Acta 84, 543-559.

Yardley, B.W.D., Rochelle, C.A., Barnicoat, A.C., Lloyd, G.E., 1991. Oscillatory zoning in metamorphic minerals: an indicator of infiltration metasomatism. Mineralogical Magazine, 55(380), 357-365.

Zack, T., John, T. 2007. An evaluation of reactive fluid flow and trace element mobility in subducting slabs. Chemical Geology 239, 199-216.

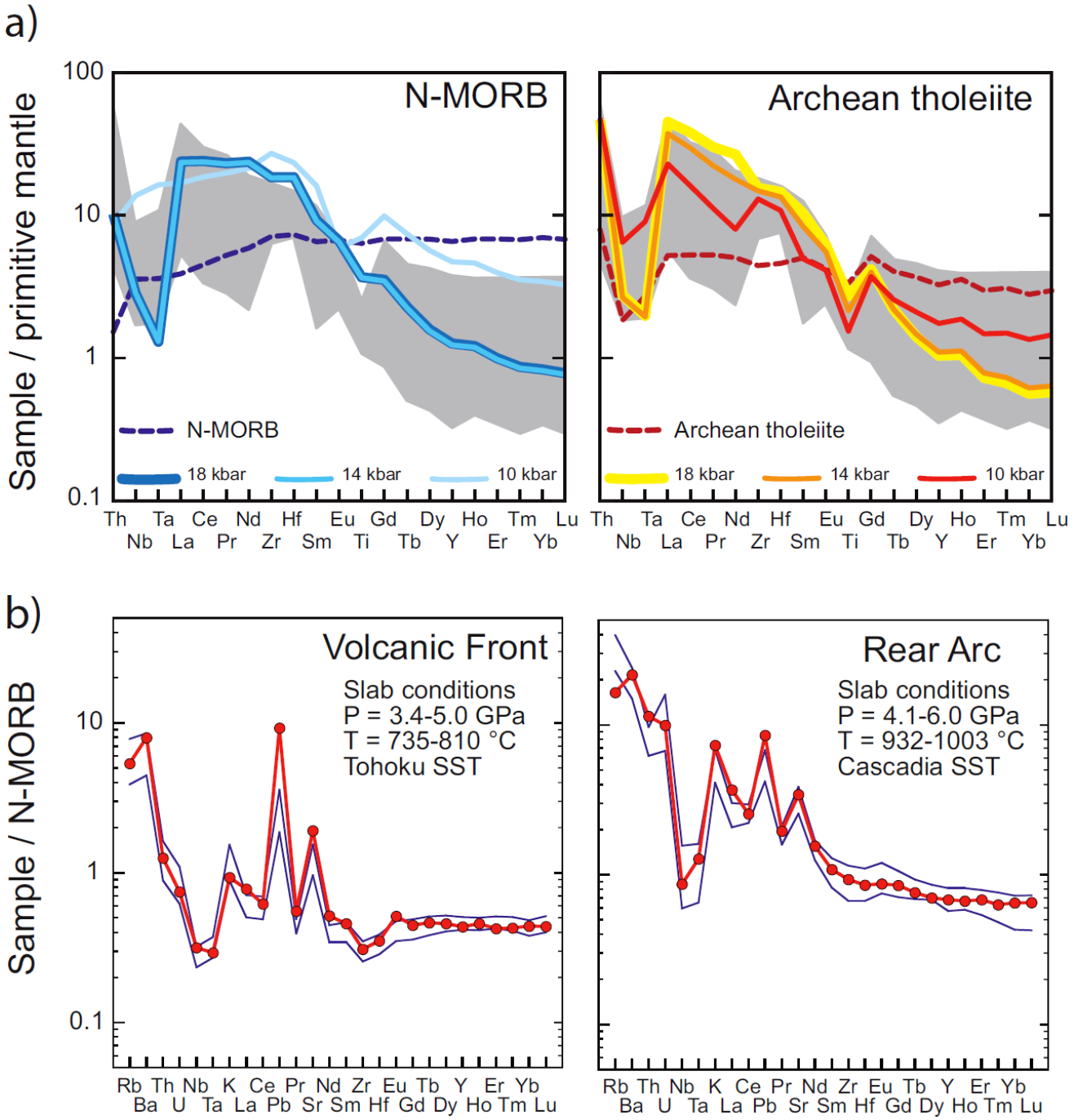
a)
Sample / primitive mantle
100
10
1
0.1
N-MORB
N-MORB
18 kbar
14 kbar
10 kbar
Archean tholeiite
Archean tholeiite
18 kbar
14 kbar
10 kbar
Th Ta Ce Nd Hf Eu Gd Dy Ho Tm Lu
Nb La Pr Zr Sm Ti Tb Y Er Yb
b)
Sample / N-MORB
10
1
0.1
Volcanic Front
Slab conditions
P = 3.4-5.0 GPa
T = 735-810 °C
Tohoku SST
Rear Arc
Slab conditions
P = 4.1-6.0 GPa
T = 932-1003 °C
Cascadia SST
Rb Th Nb K Ce Pr Nd Zr Eu Tb Y Er Yb
Ba U Ta La Pb Sr Sm Hf Gd Dy Ho Tm Lu

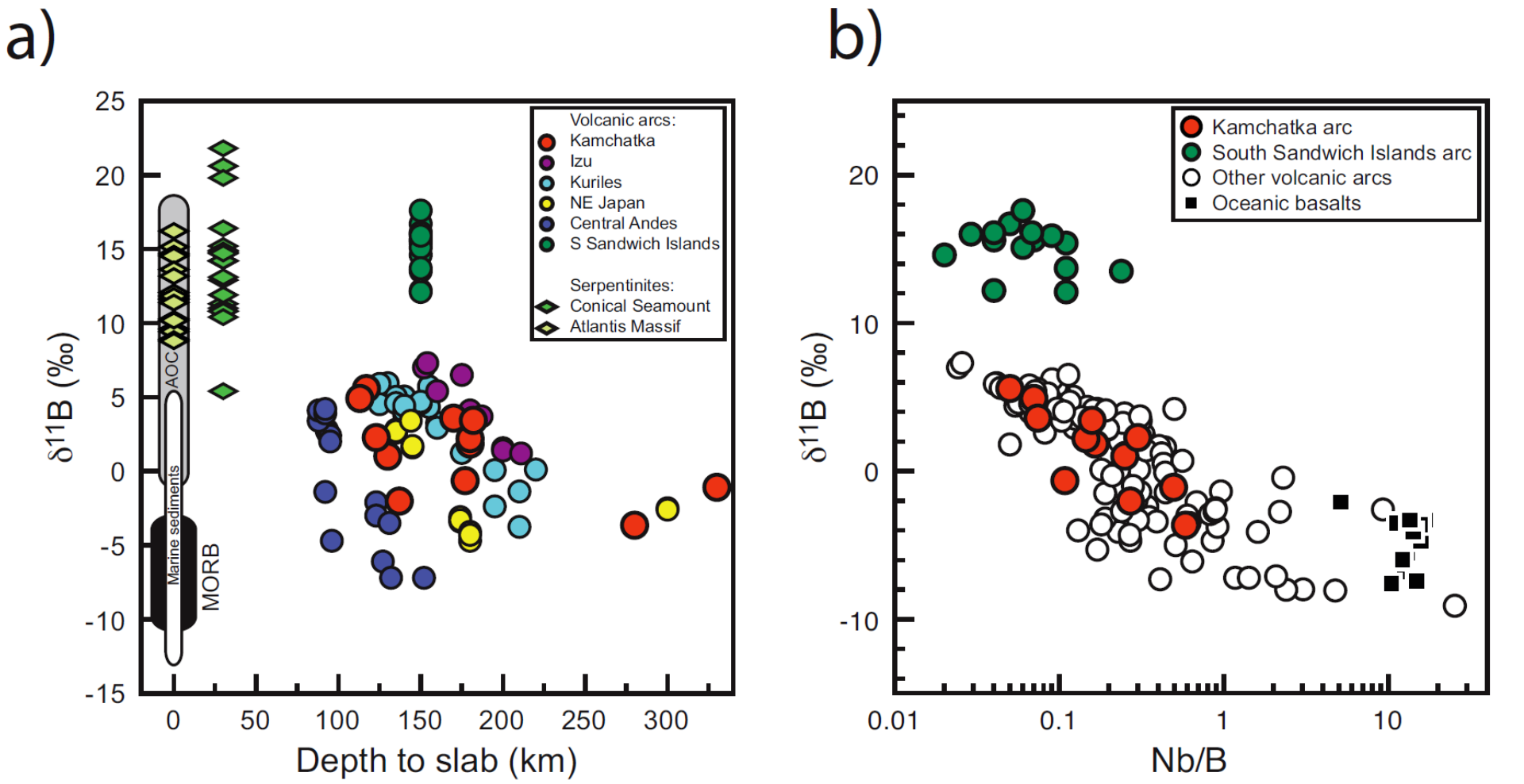
a)
b)
δ11B (‰)
Depth to slab (km)
Nb/B
Volcanic arcs:
Kamchatka
Izu
Kuriles
NE Japan
Central Andes
S Sandwich Islands
Serpentinites:
Conical Seamount
Atlantis Massif
AOC
Marine sediments
MORB
Kamchatka arc
South Sandwich Islands arc
Other volcanic arcs
Oceanic basalts

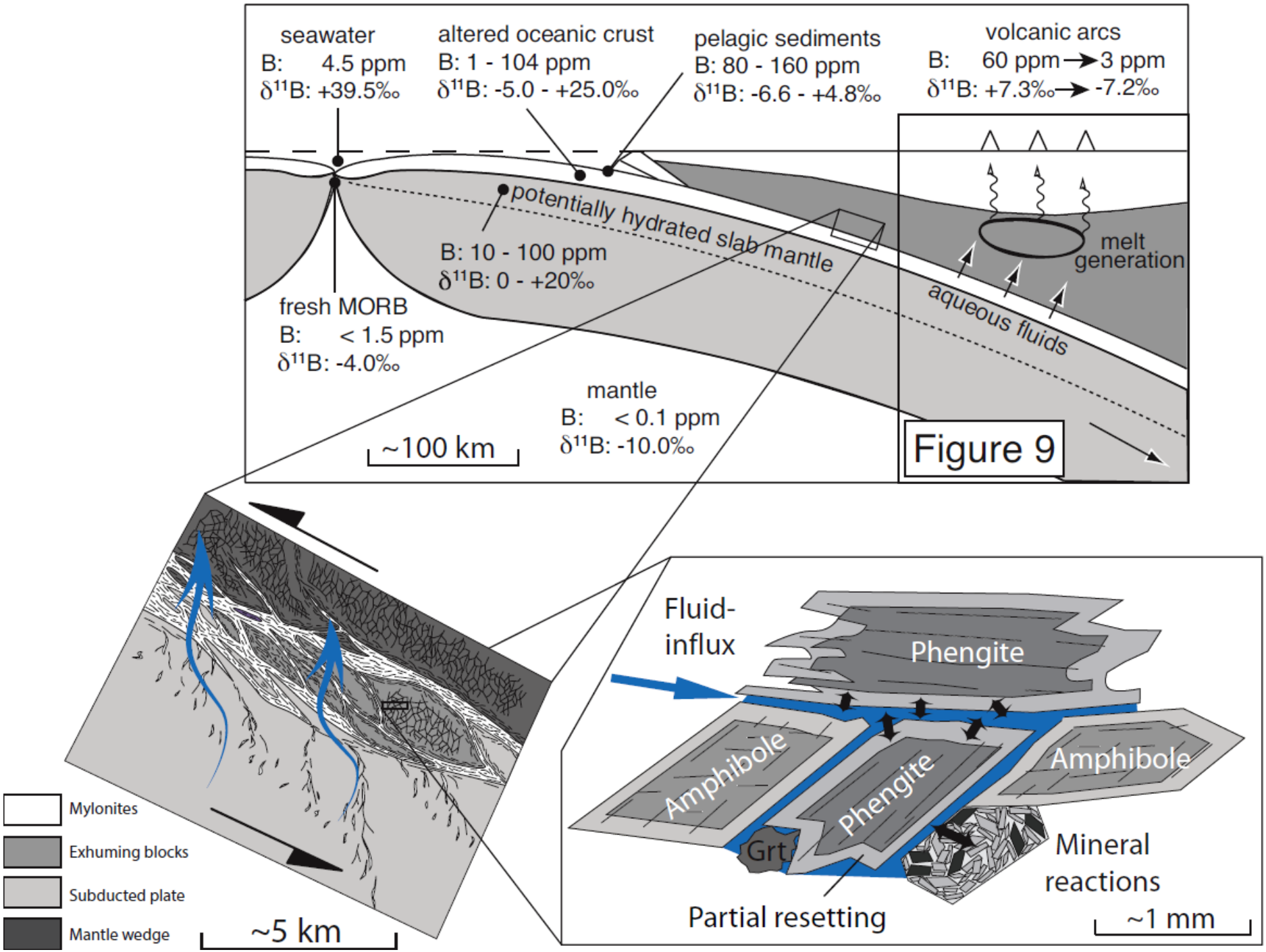
seawater
B: 4.5 ppm
δ11B: +39.5‰
altered oceanic crust
B: 1 - 104 ppm
δ11B: -5.0 - +25.0‰
pelagic sediments
B: 80 - 160 ppm
δ11B: -6.6 - +4.8‰
volcanic arcs
B: 60 ppm → 3 ppm
δ11B: +7.3‰ → -7.2‰
potentially hydrated slab mantle
B: 10 - 100 ppm
δ11B: 0 - +20‰
fresh MORB
B: < 1.5 ppm
δ11B: -4.0‰
mantle
B: < 0.1 ppm
δ11B: -10.0‰
melt generation
aqueous fluids
~100 km
Figure 9
Mylonites
Exhuming blocks
Subducted plate
Mantle wedge
~5 km
Fluid-influx
Phengite
Amphibole
Phengite
Amphibole
Grt
Partial resetting
Mineral reactions
~1 mm

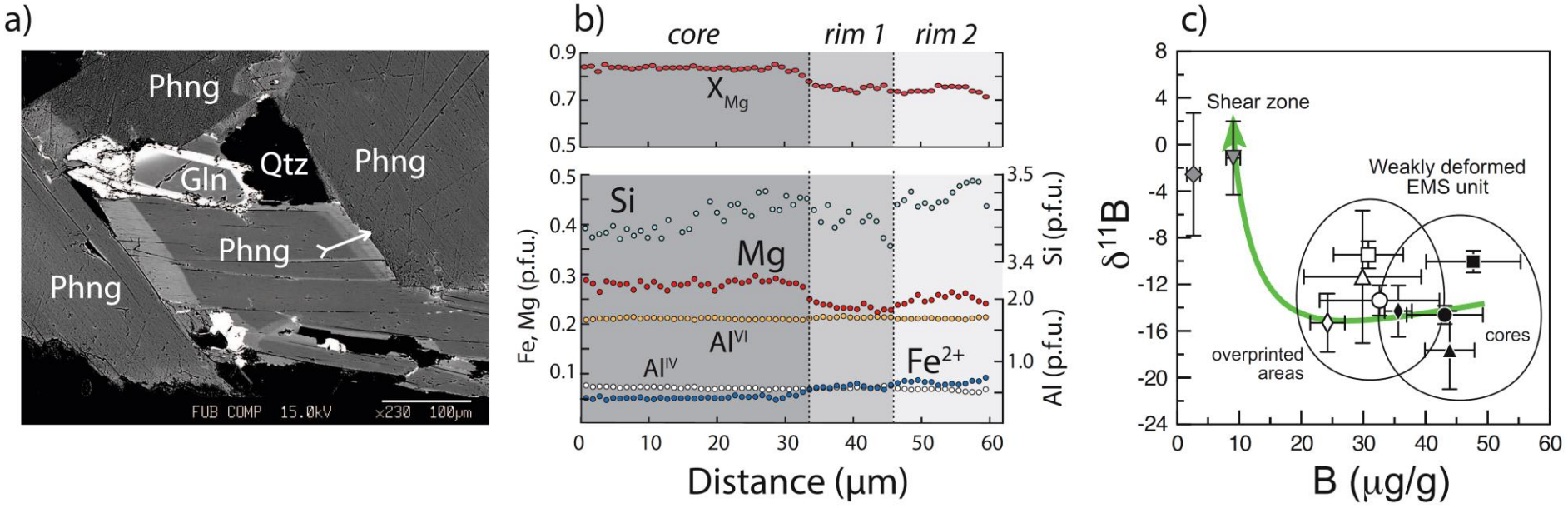
a)
Phng
Qtz
Gln
Phng
Phng
Phng
FUB COMP 15.0kV ×230 100µm
b)
core
rim 1
rim 2
X_Mg
Si
Mg
Al^VI
Al^IV
Fe^2+
Fe, Mg (p.f.u.)
Si (p.f.u.)
Al (p.f.u.)
Distance (µm)
c)
Shear zone
Weakly deformed EMS unit
overprinted areas
cores
δ11B
B (µg/g)

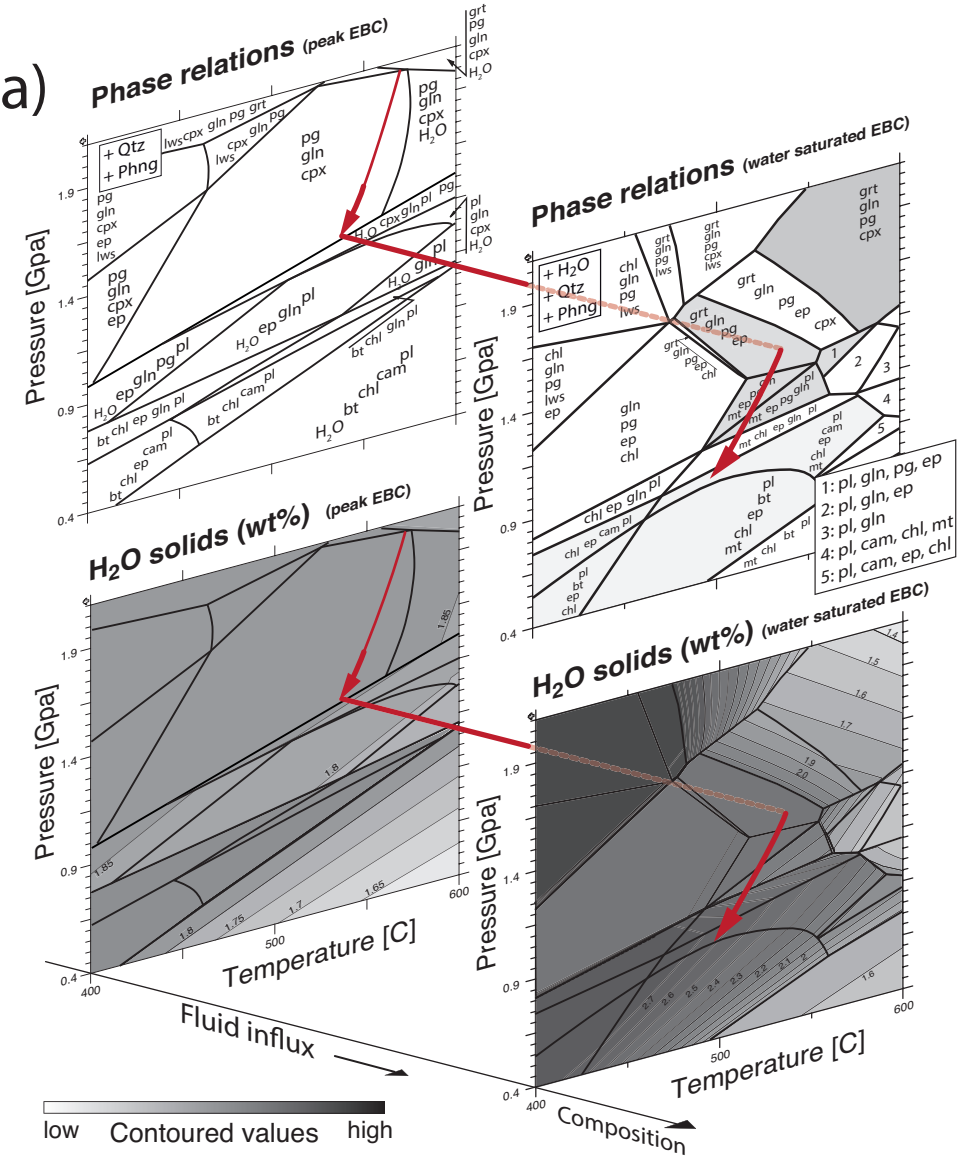
a)
Phase relations (peak EBC)
Phase relations (water saturated EBC)
H2O solids (wt%) (peak EBC)
H2O solids (wt%) (water saturated EBC)
Pressure [Gpa]
Temperature [C]
Fluid influx
Composition
low
Contoured values
high
1: pl, gln, pg, ep
2: pl, gln, ep
3: pl, gln
4: pl, cam, chl, mt
5: pl, cam, ep, chl

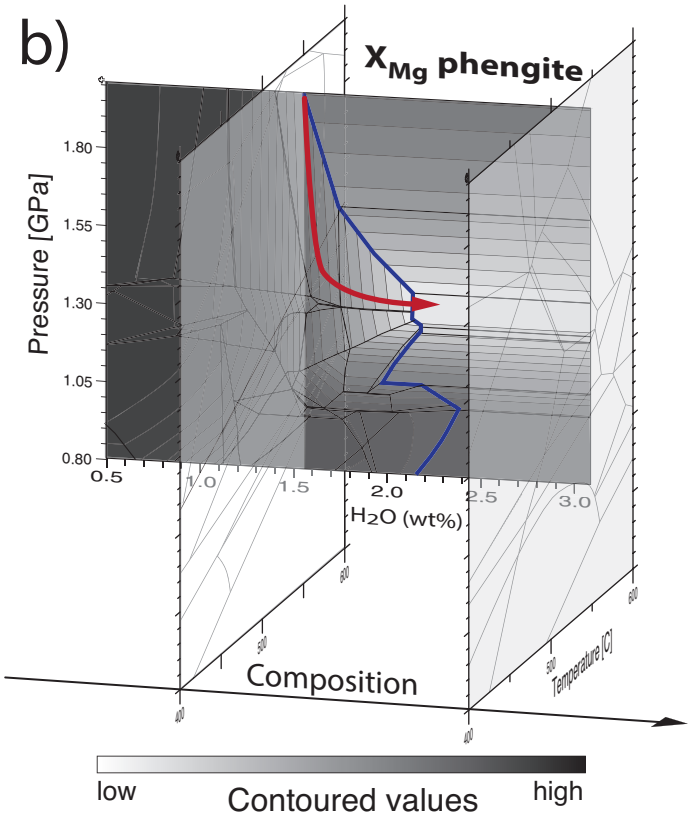
b)
XMg phengite
Pressure [GPa]
H2O (wt%)
Composition
Temperature [C]
low
Contoured values
high

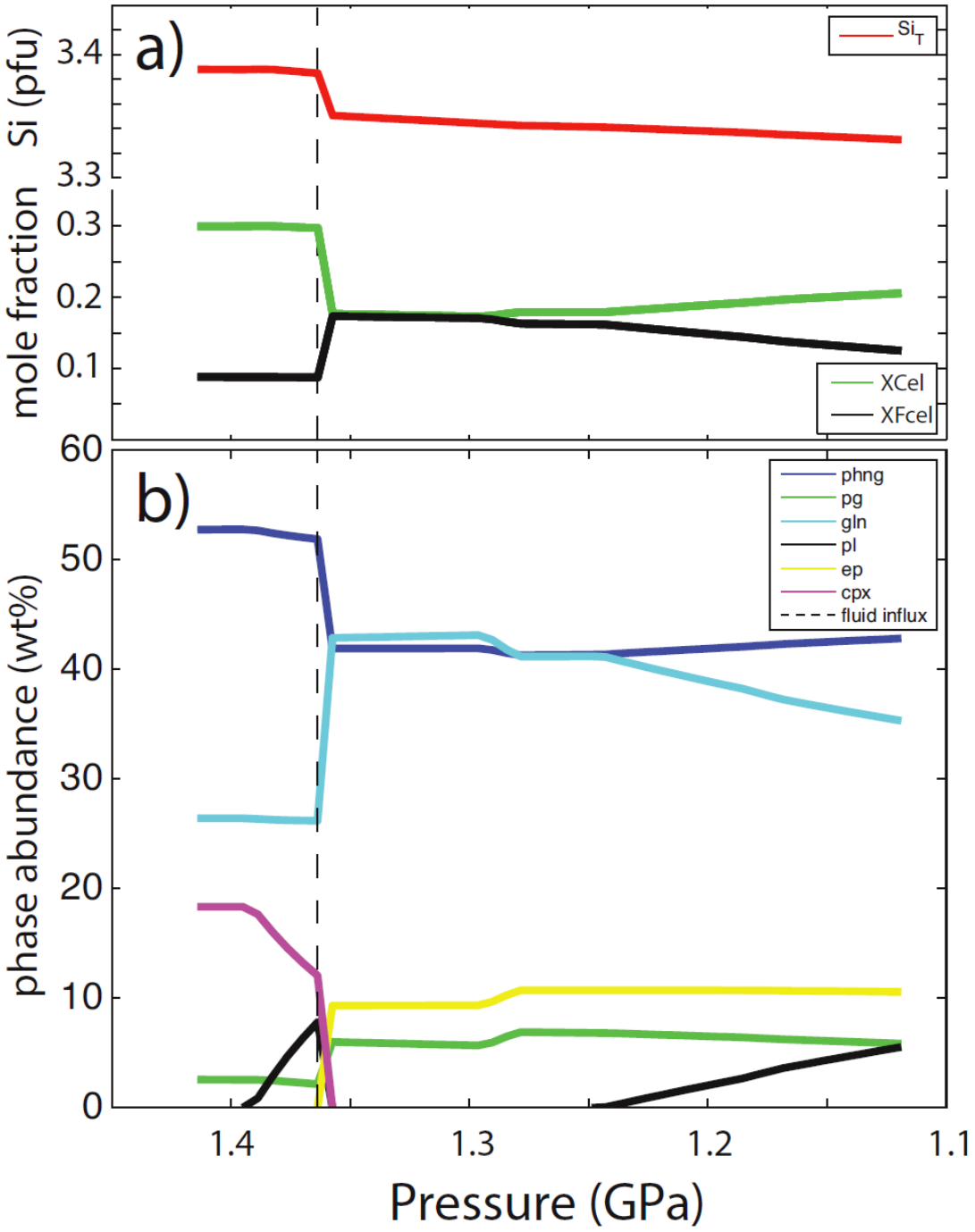
a)
Si (pfu)
3.4
3.3
mole fraction
0.3
0.2
0.1
0
Si$_T$
XCel
XFcel
b)
phase abundance (wt%)
60
50
40
30
20
10
0
phng
pg
gln
pl
ep
cpx
fluid influx
1.4
1.3
1.2
1.1
Pressure (GPa)

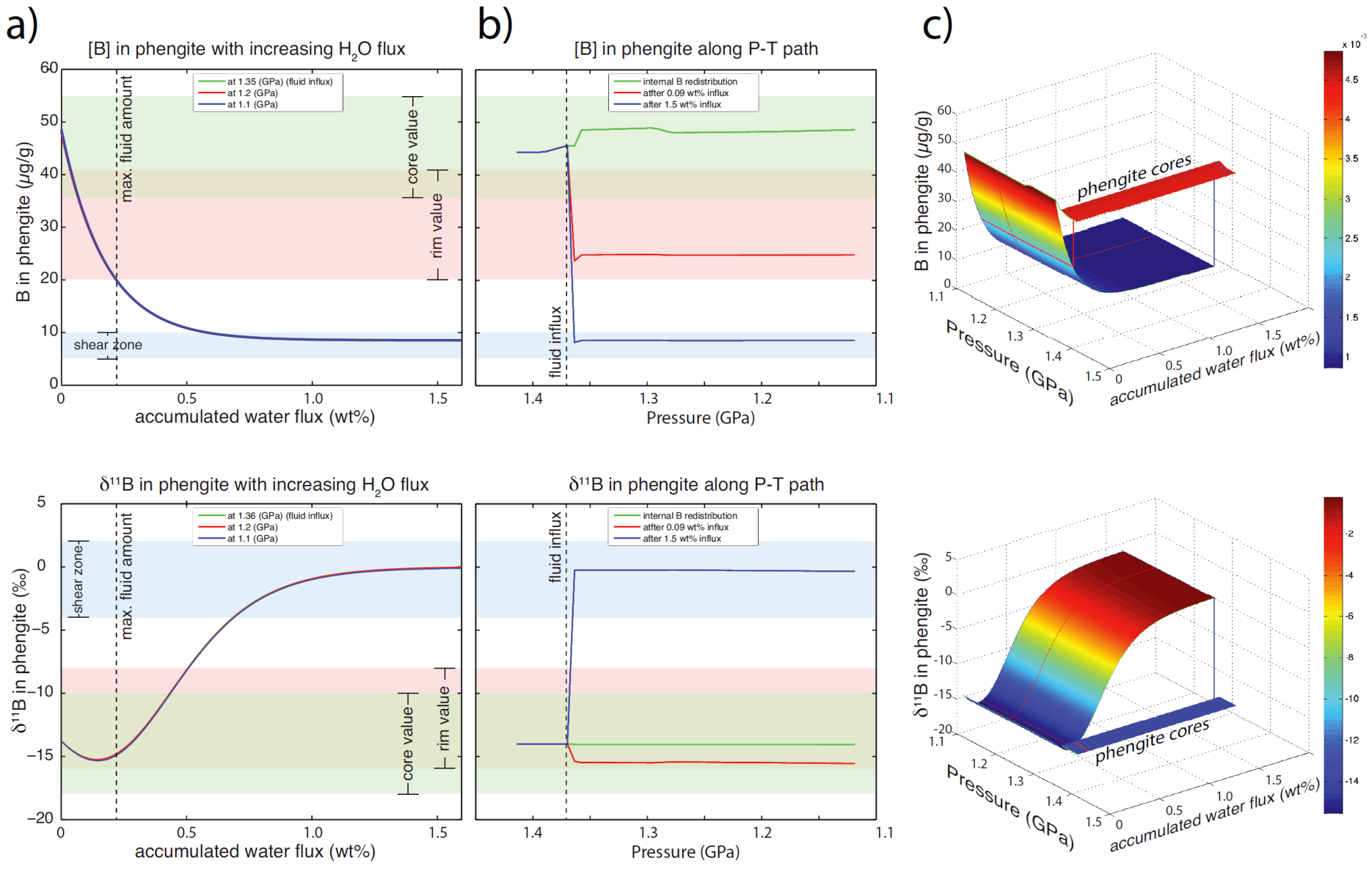
a)
[B] in phengite with increasing H2O flux
B in phengite (µg/g)
accumulated water flux (wt%)
at 1.35 (GPa) (fluid influx)
at 1.2 (GPa)
at 1.1 (GPa)
max. fluid amount
shear zone
core value
rim value
b)
[B] in phengite along P-T path
Pressure (GPa)
internal B redistribution
atfter 0.09 wt% influx
after 1.5 wt% influx
fluid influx
c)
B in phengite (µg/g)
phengite cores
Pressure (GPa)
accumulated water flux (wt%)
δ11B in phengite with increasing H2O flux
δ11B in phengite (‰)
at 1.36 (GPa) (fluid influx)
δ11B in phengite along P-T path
δ11B in phengite (‰)

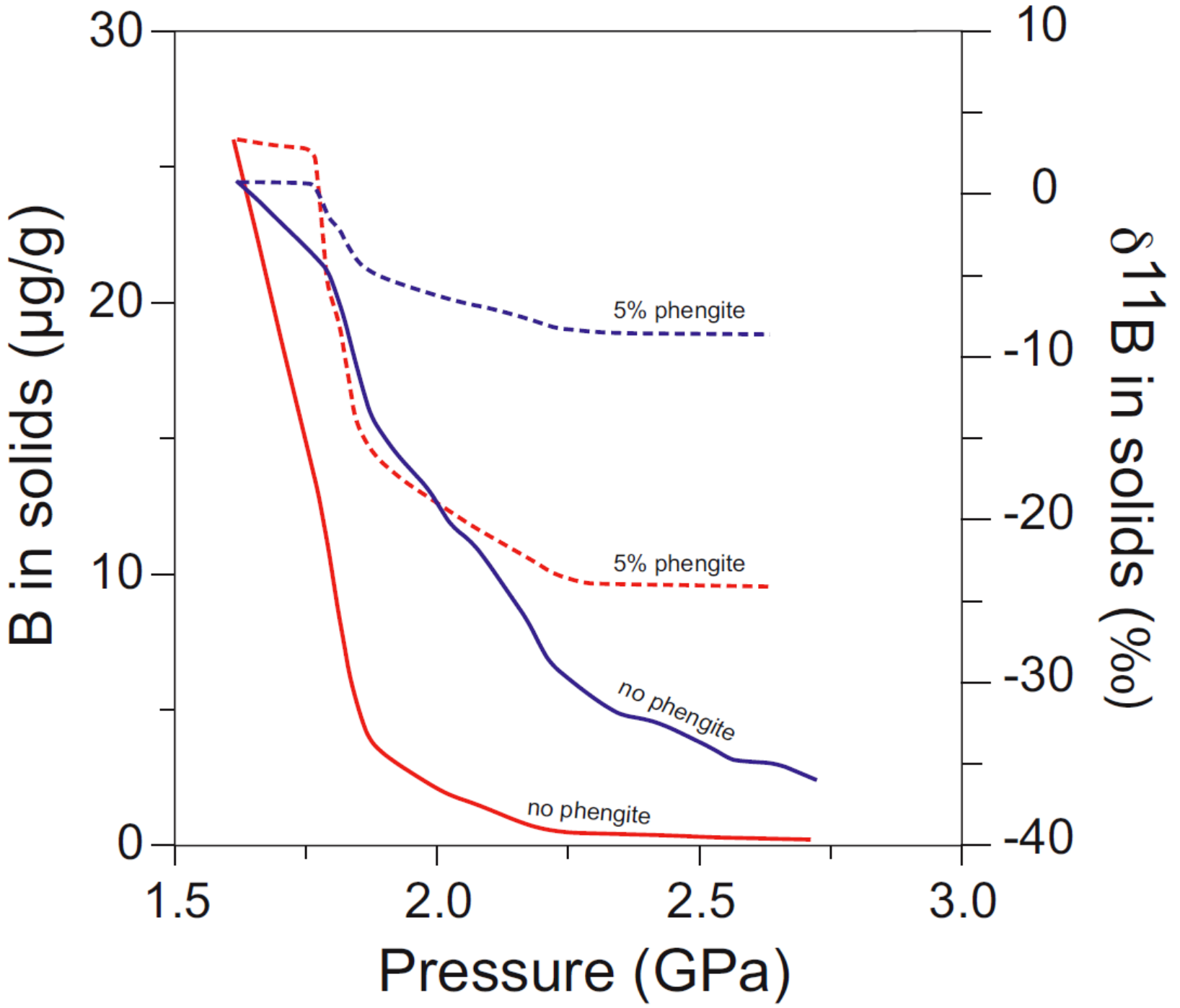
30
20
10
0
10
0
-10
-20
-30
-40
1.5
2.0
2.5
3.0
B in solids (µg/g)
δ11B in solids (‰)
Pressure (GPa)
5% phengite
5% phengite
no phengite
no phengite

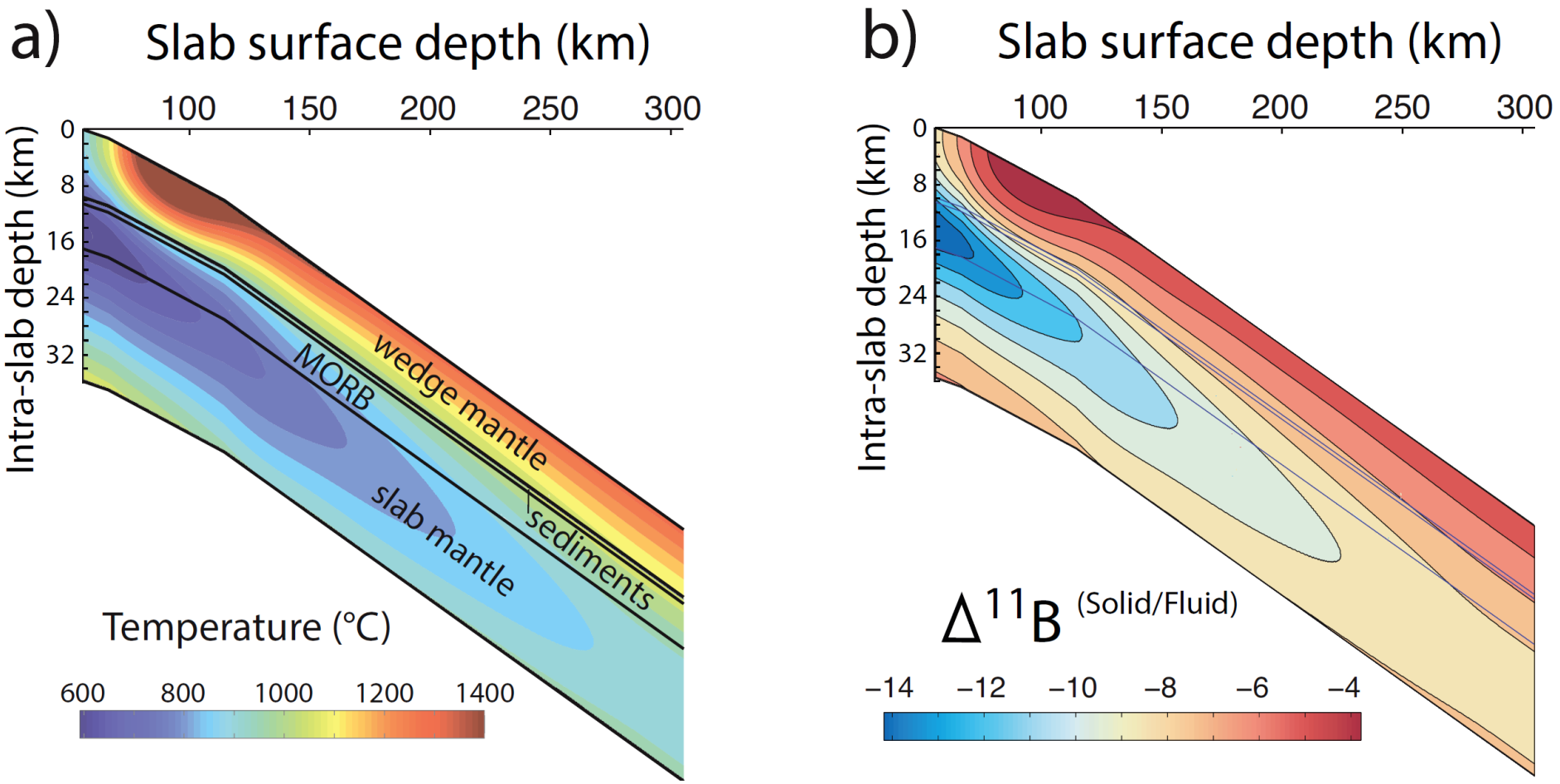
a)
Slab surface depth (km)
100
150
200
250
300
Intra-slab depth (km)
0
8
16
24
32
wedge mantle
MORB
slab mantle
sediments
Temperature (°C)
600
800
1000
1200
1400
b)
Slab surface depth (km)
100
150
200
250
300
Intra-slab depth (km)
0
8
16
24
32
Δ11B (Solid/Fluid)
−14
−12
−10
−8
−6
−4

a)

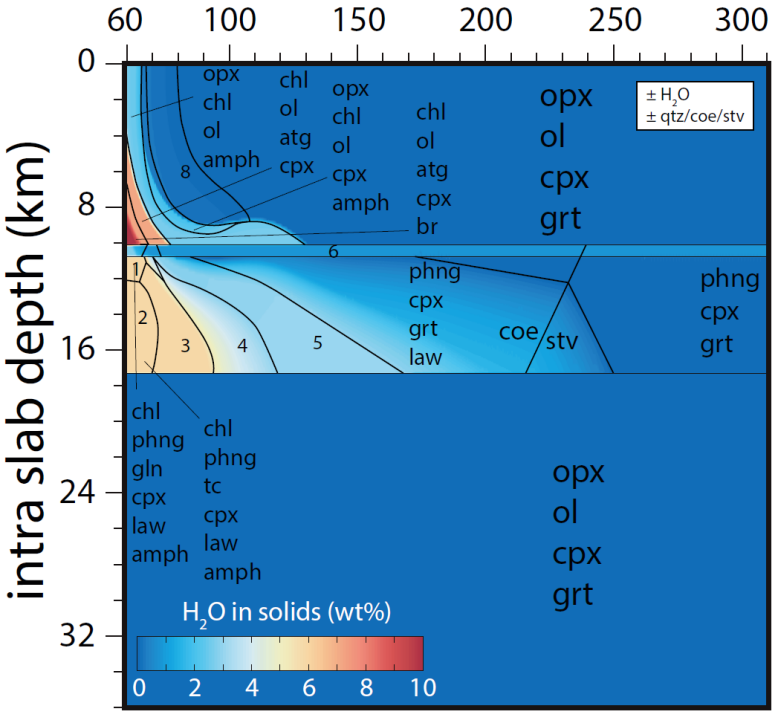

1: chl phng gln cpx law amph
2: chl phng tc cpx law amph
3: chl phng tc cpx law
4: chl phng tc cpx grt law
5: tc cpx grt law phng
6: phng cpx grt
7: chl phng cpx law
8: opx ol cpx grt amph

b)

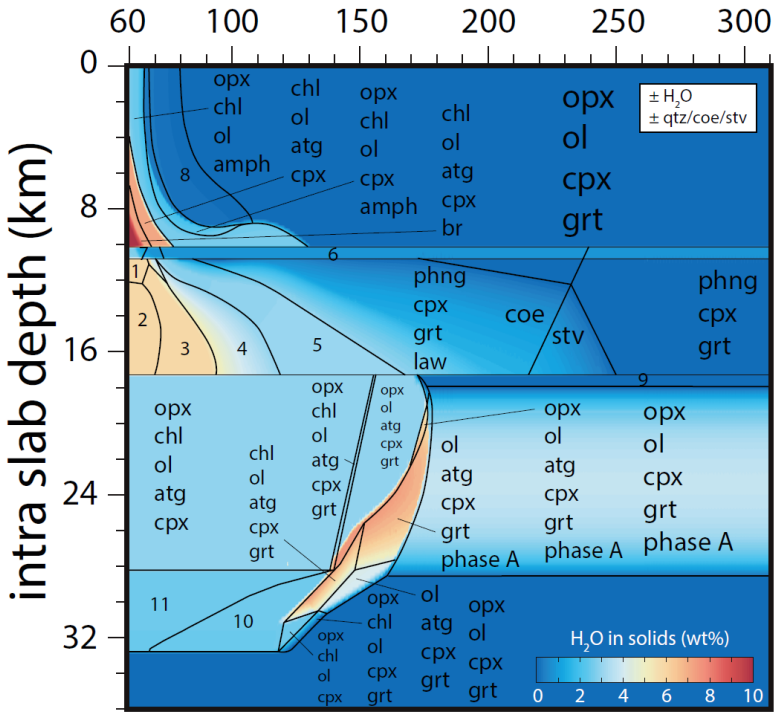

1: chl phng gln cpx law amph
2: chl phng tc cpx law amph
3: chl phng tc cpx law
4: chl phng tc cpx grt law
5: tc cpx grt law phng
6: phng cpx grt
7: chl phng cpx law
8: opx ol cpx grt amph
9: opx ol cpx grt
10: opx chl ol cpx grt
11: opx chl ol cpx

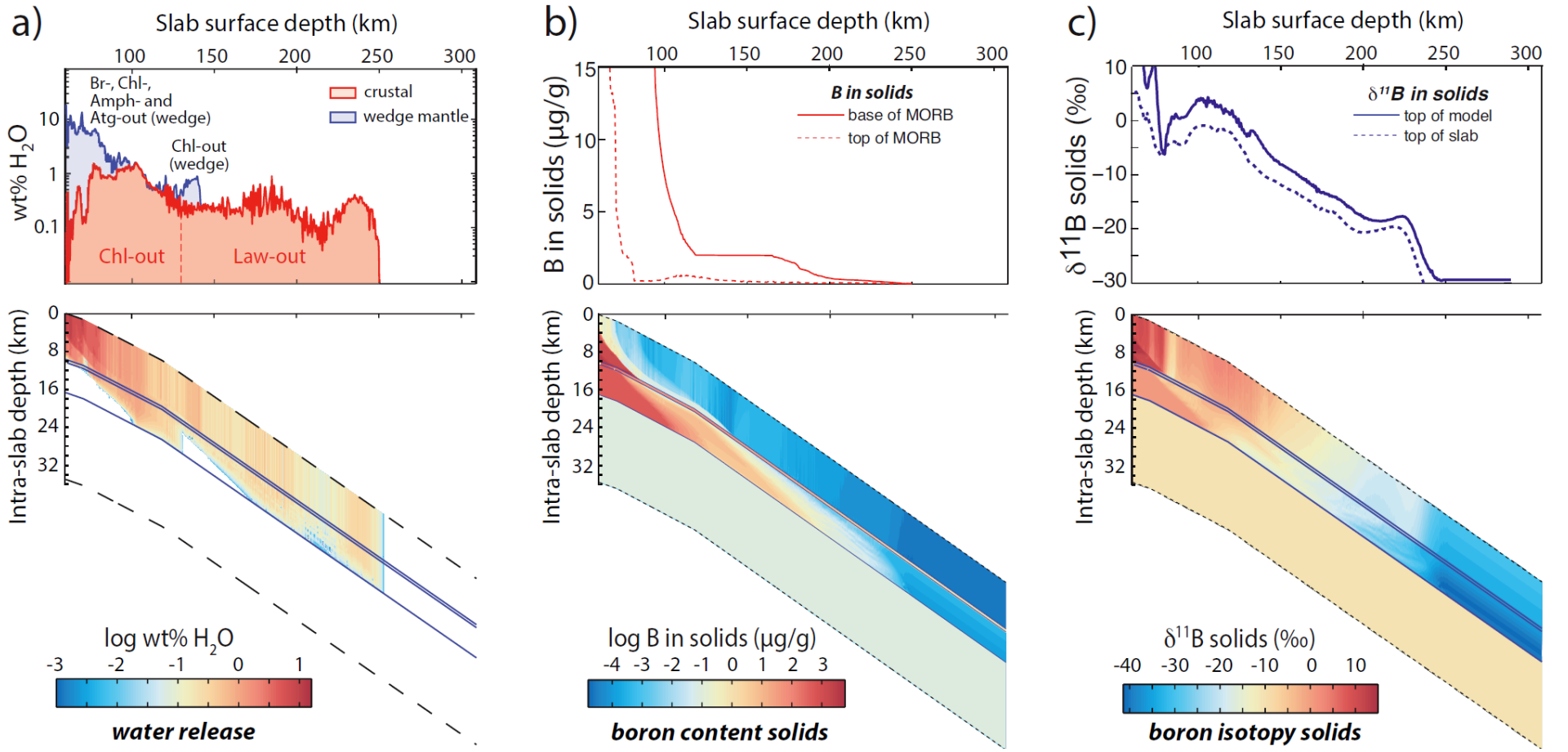
a)
Slab surface depth (km)
100
150
200
250
300
wt% H2O
10
1
0.1
Br-, Chl-,
Amph- and
Atg-out (wedge)
Chl-out
(wedge)
crustal
wedge mantle
Chl-out
Law-out
Intra-slab depth (km)
0
8
16
24
32
log wt% H2O
-3
-2
-1
0
1
water release
b)
Slab surface depth (km)
100
150
200
250
300
B in solids (µg/g)
15
10
5
0
B in solids
base of MORB
top of MORB
Intra-slab depth (km)
log B in solids (µg/g)
-4
-3
-2
-1
0
1
2
3
boron content solids
c)
Slab surface depth (km)
100
150
200
250
300
δ11B solids (‰)
10
0
−10
−20
−30
δ11B in solids
top of model
top of slab
Intra-slab depth (km)
δ11B solids (‰)
-40
-30
-20
-10
0
10
boron isotopy solids

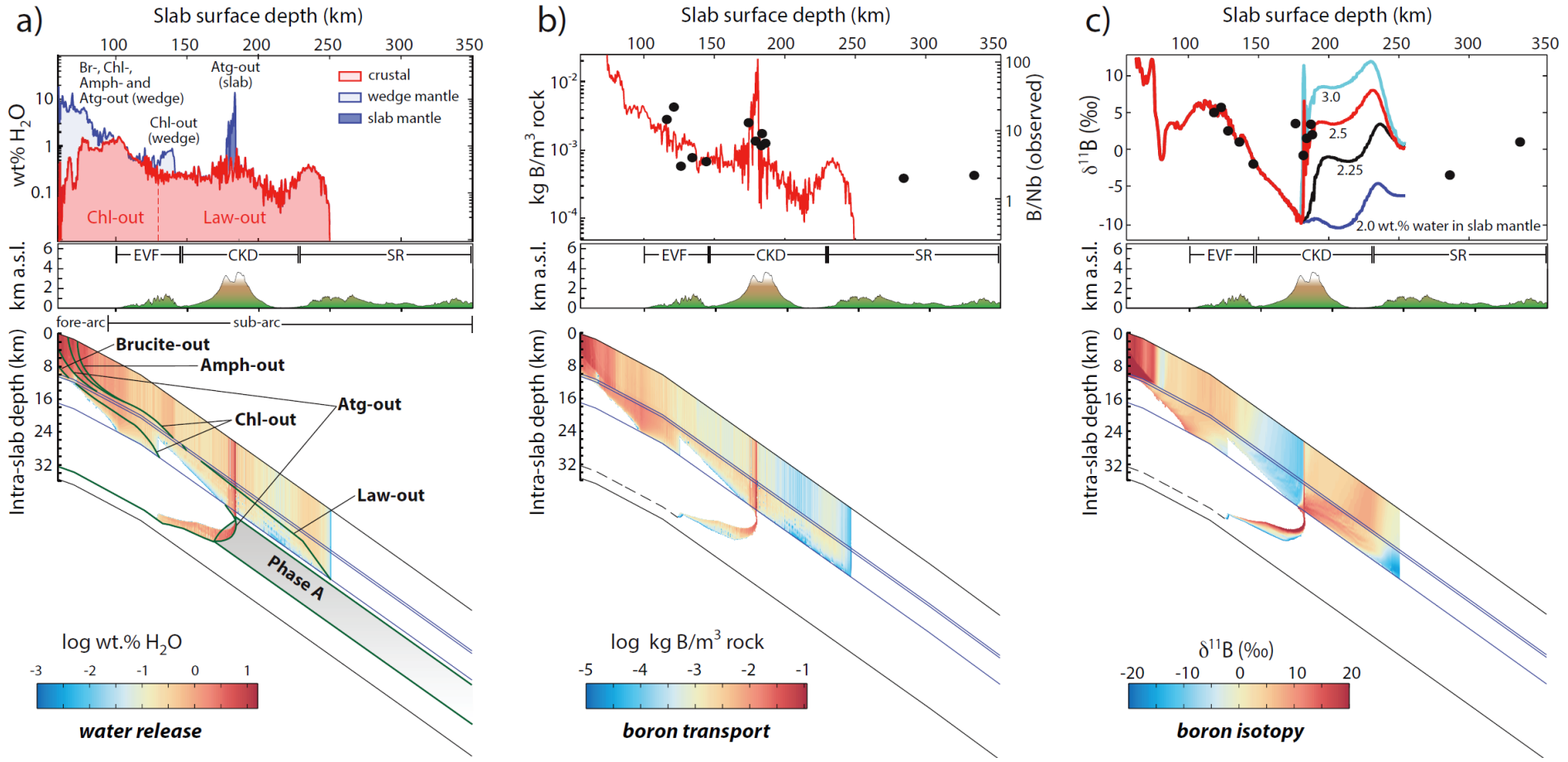
a)
Slab surface depth (km)
100 150 200 250 300 350
wt% H2O
Br-, Chl-, Amph- and Atg-out (wedge)
Chl-out (wedge)
Atg-out (slab)
crustal
wedge mantle
slab mantle
Chl-out
Law-out
km a.s.l.
EVF
CKD
SR
fore-arc
sub-arc
Intra-slab depth (km)
Brucite-out
Amph-out
Atg-out
Chl-out
Law-out
Phase A
log wt.% H2O
water release
b)
Slab surface depth (km)
kg B/m3 rock
B/Nb (observed)
log kg B/m3 rock
boron transport
c)
Slab surface depth (km)
δ11B (‰)
3.0
2.5
2.25
2.0 wt.% water in slab mantle
δ11B (‰)
boron isotopy

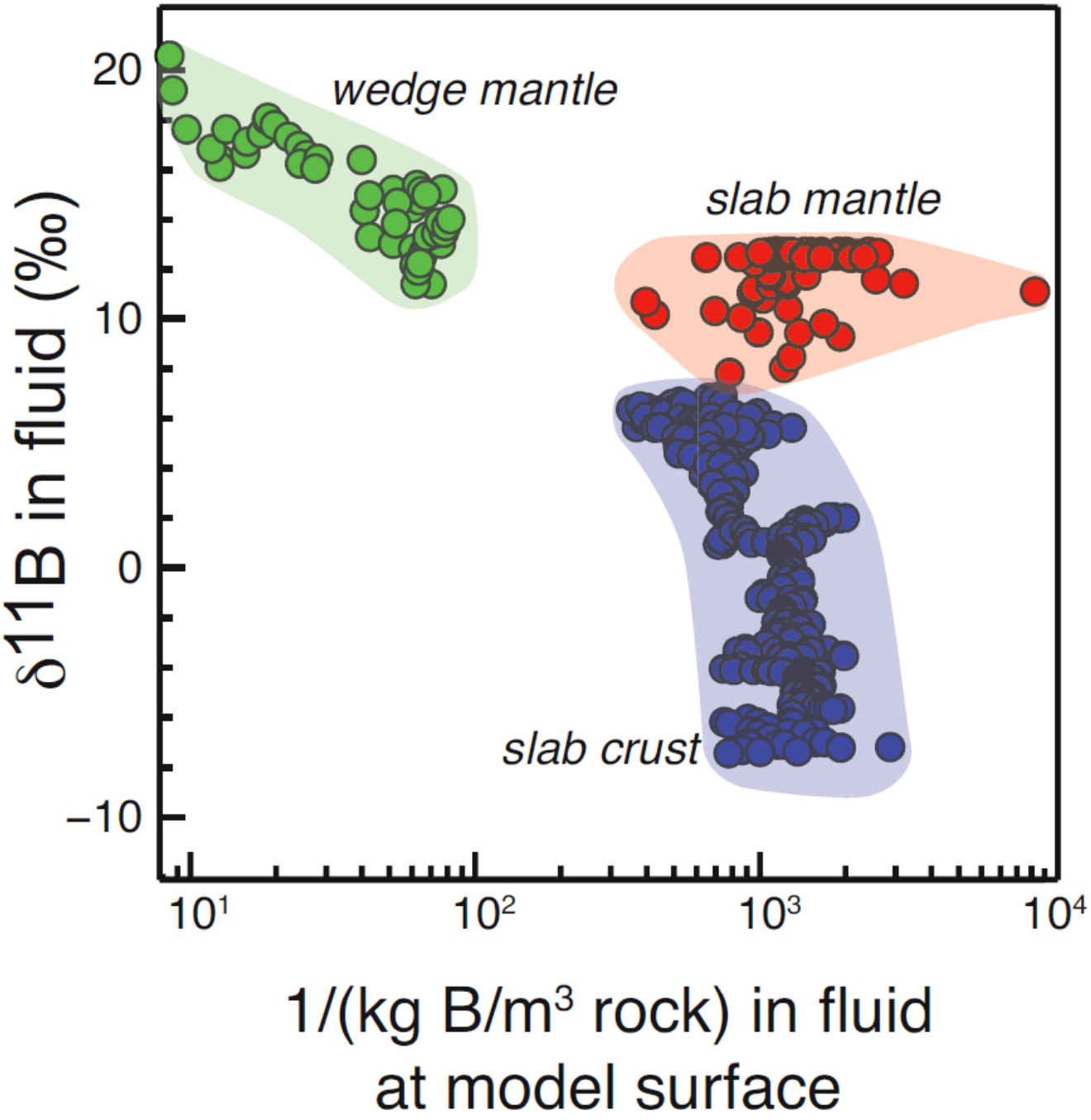
wedge mantle
slab mantle
slab crust
20
10
0
−10
δ11B in fluid (‰)
10¹
10²
10³
10⁴
1/(kg B/m³ rock) in fluid
at model surface

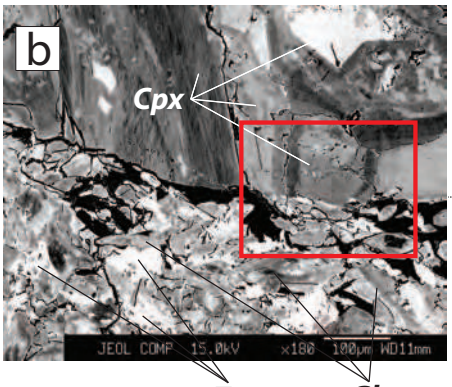

Eclogite
cpx + grt + rt

reaction front

Blueschist
gln + tn + plag

m-scale

mm-scale

µm-scale

nm-scale

Tn

Gln

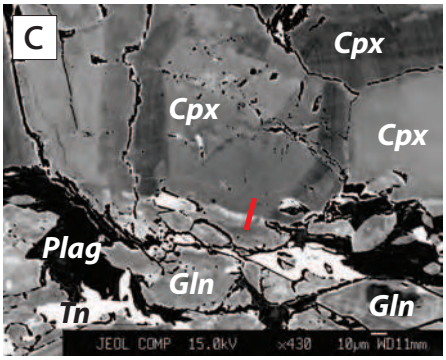

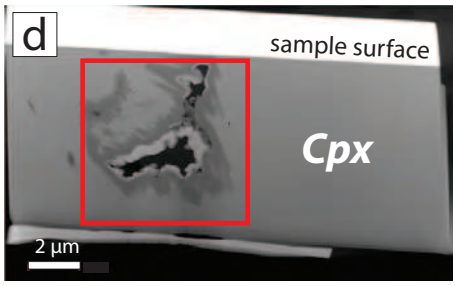

Ga precipitate (from FIB)

amorphous overprinting zone

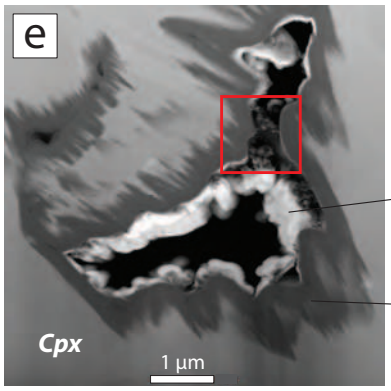

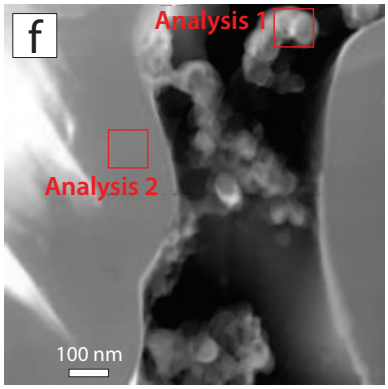

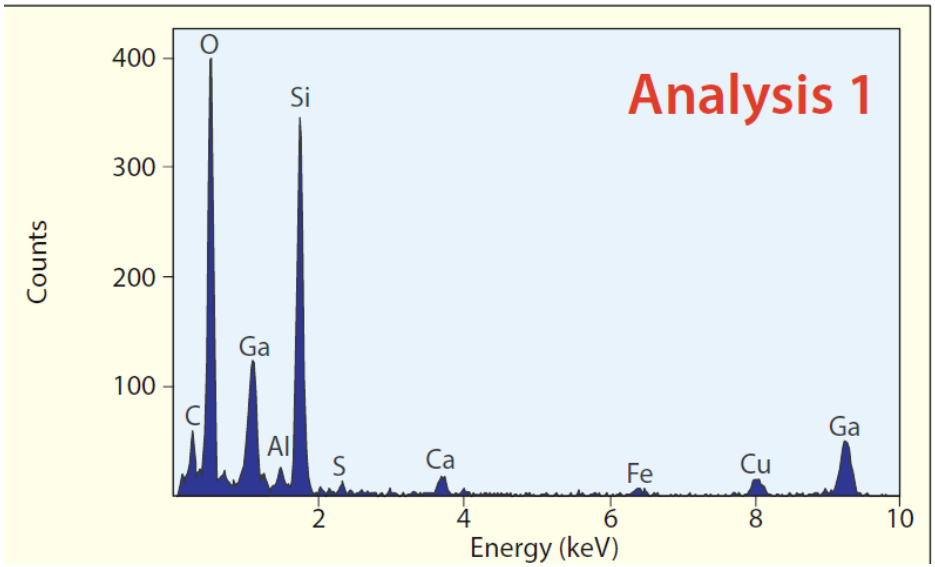
Analysis 1
Counts
Energy (keV)
O
Si
Ga
C
Al
S
Ca
Fe
Cu
Ga
400
300
200
100
2
4
6
8
10

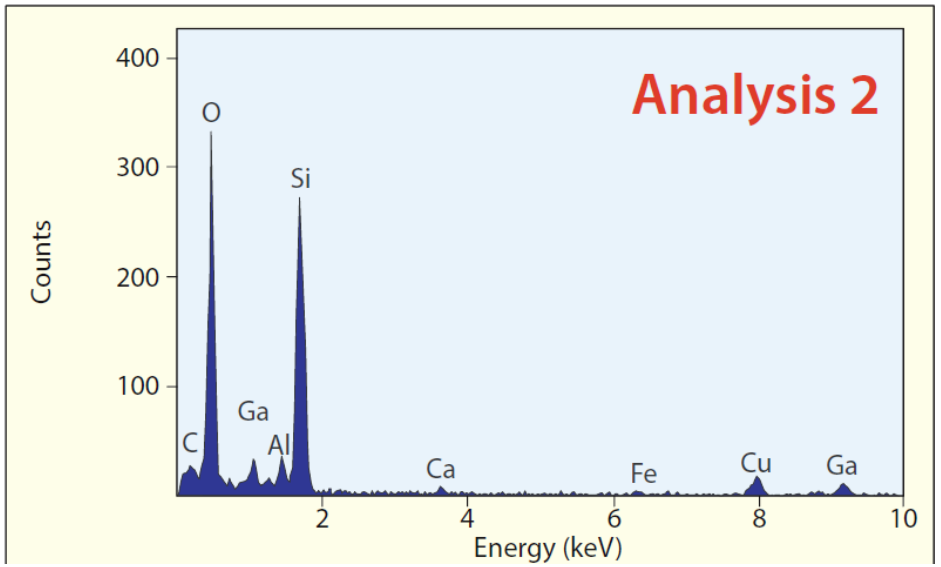
Analysis 2
Counts
Energy (keV)
O
Si
Ga
C
Al
Ca
Fe
Cu
Ga
400
300
200
100
2
4
6
8
10